Far-Infrared and Millimeter Continuum Studies of K-Giants: α Boo and α Tau

Martin Cohen

Radio Astronomy Laboratory, 601 Campbell Hall, University of California, Berkeley, CA 94720

Electronic mail: mcohen@astro.berkeley.edu

Duane F. Carbon

NASA/Ames Research Center, Mailstop 258-5, Moffett Field, CA 94035-1000

Electronic mail: dcarbon@nas.nasa.gov

William J. Welch

Radio Astronomy Laboratory, 601 Campbell Hall, University of California, Berkeley, CA 94720

Electronic mail: welch@jack.berkeley.edu

Tanya Lim

Space Science Department, Rutherford Appleton Laboratory, Chilton, Didcot OX11 0QX, UK

Electronic mail: T.L.Lim@rl.ac.uk

James R. Forster

Hat Creek Observatory, University of California, 42331 Bidwell Road, Hat Creek, CA 96040

Electronic mail: rforster@astro.berkeley.edu

David Goorvitch

NASA/Ames Research Center, Mailstop 245-6, Moffett Field, CA 94035-1000

Electronic mail: goorvit@ssa1.arc.nasa.gov

Received ____________________; accepted ____________________

ABSTRACT

We have imaged two normal, non-coronal, infrared-bright K-giants, α Boo and α Tau, in the 1.4-mm and 2.8-mm continuum using BIMA. These stars have been used as important absolute calibrators for several infrared satellites. Our goals are: (1) to probe the structure of their upper photospheres; (2) to establish whether these stars radiate as simple photospheres or possess long-wavelength chromospheres; and (3) to make a connection between millimeter-wave and far-infrared absolute flux calibrations. To accomplish these goals we also present ISO Long Wavelength Spectrometer (LWS) measurements of both these K-giants. The far-infrared and millimeter continuum radiation is produced in the vicinity of the temperature minimum in α Boo and α Tau, offering a direct test of the model photospheres and chromospheres for these two cool giants. We find that current photospheric models predict fluxes in reasonable agreement with those observed for those wavelengths which sample the upper photosphere, namely $\leq$170 μm in α Tau and $\leq$125 μm in α Boo. It is possible that α Tau is still radiative as far as 0.9 - 1.4 mm. We detect chromospheric radiation from both stars by 2.8 mm (by 1.4 mm in α Boo), and are able to establish useful bounds on the location of the temperature minimum. An attempt to interpret the chromospheric fluxes using the two-component "bifurcation model" proposed by Wiedemann et al. (1994) appears to lead to a significant contradiction.

Subject headings: infrared: radiation — infrared: stars — stars: atmospheres — stars: chromospheres — stars: individual(α Boo, α Tau) — techniques: photometric

1. Introduction

We had several distinct objectives in undertaking this work, dominantly to study the atmospheric structure in normal K-giants, but secondarily to investigate the merit and reliability of such stars as absolute far-infrared and millimeter calibration sources.

1.1. Cool stellar atmospheres

Our primary goal is to probe the structure of the outer atmospheres in K and, eventually, M giants. Vernazza et al. (1976) demonstrated in a classic paper how observations of the far-infrared continua, atomic lines, and UV continua could be brought together to construct a single-component, time-independent mean solar temperature structure. Far-infrared continuum fluxes were of crucial importance in helping to establish the mean solar temperature structure from the upper photosphere, through the temperature minimum region, and into the chromosphere. Our intent is to use the far-infrared and millimeter fluxes of selected red giants to probe their outer layers in the same fashion in order to test models of the stellar photospheres and chromospheres. This is possible because the primary infrared continuous opacity, H^- free-free, increases as λ^2, pushing the depth of continuum formation into the outermost stellar layers. Until now these layers have been accessible only through non-LTE analyses of the cores of strong atomic and molecular lines (e.g., Ayres & Linsky (1975), Kelch et al. (1978), McMurry (1999), Wiedemann et al. (1994)). We are particularly interested in determining the location of the transition from the purely radiative equilibrium upper photosphere to the non-radiatively heated chromosphere. In addition, we wish to trace the run of decreasing temperatures through the upper photosphere and determine how closely current stellar model atmosphere calculations can predict this run. This information on the location of the temperature reversal and the quality of fit to the fluxes originating in the upper photosphere is vital in defining the wavelength range for which radiative models may be used for far-infrared calibrations. Finally, we wish to provide far-infrared and millimeter fluxes which may be used to constrain stellar chromospheric models. We have chosen α Boo and α Tau for this initial study because these stars, being both bright and nearby, are easily the two most completely and thoroughly studied red giants. This makes them the ideal test cases for our purposes. It should be noted that they both lie on the cool, non-coronal side of the "Linsky-Haisch dividing line" (Linsky & Haisch 1979) which separates coronal from non-coronal giants, although Ayres et al (1997) have recently found evidence for buried high temperature emission in the case of α Boo.

1.2. Infrared calibration stars

Cohen and colleagues have presented a self-consistent context for absolute calibration in the infrared, suitable for use by ground-based, airborne, and spaceborne spectrometers and radiometers (Cohen et al. 1992a,b,c, 1995; Cohen & Davies 1995; Cohen et al. 1996a,b, 1999). This context is based upon a pair of absolutely calibrated, infrared-customized models of Vega and Sirius calculated by Kurucz. These efforts have furnished the absolute stellar spectrum of Sirius that underpins COBE/DIRBE bands 1–5 (Mitchell et al. 1996; Cohen 1998) and the spectra of K0-M0IIIs for the on-orbit calibration of the Near- and Mid-Infrared Spectrometers on the joint NASA/ISAS Infrared Telescope in Space (Murakami et al. 1997), likewise for ESA's Infrared Space Observatory (ISO) (Kessler et al. 1996) instruments (e.g., the Short Wavelength Spectrometer: Schaeidt et al. (1996) and for the Spatial InfraRed Imaging Telescope (SPIRIT-III) on the US Midcourse Space Experiment (Mill et al. 1994).

The absolute calibration of ISOPHOT (Lemke et al. 1996; Schulz et al. 2001) was supported by planets, asteroids, and stars, ranked in order of decreasing flux density

(Muller & Lagerros 1998; Schulz et al. 2001). The stellar calibrators (Cohen et al. 1996b) necessitated long-wavelength extrapolations, as far as 200 μm, of the observed (1.2–35 μm) absolute stellar spectra by state-of-the-art model atmosphere spectra (computed by one of us [DFC]: Cohen et al. (1996b)). We note that the bright, secondary reference stars that have been selected for infrared calibration purposes are precisely those "quiet" giants in which it was suggested that radiatively-cooled regions very largely dominate the stellar surfaces so that single component atmospheric models were most likely to be valid. Examples of these are α Boo, α Hya, α Tau, and γ Dra (Wiedemann et al. 1994). Consequently, one of our objectives is to establish whether these stars radiate as expected, thereby validating the scheme used for ISO at the longest wavelengths, or possess long-wavelength chromospheres.

1.3. Linking infrared and millimetric calibration

The ISO Long Wavelength Spectrometer (LWS) (Clegg et al. 1996; Swinyard et al. 1996) used Uranus as a calibration standard but also observed Neptune, and Mars when it became available. Although Uranus has remained the LWS primary calibrator, the Mars spectrum has been shown to be fully consistent with this Uranus framework (Sidher et al. 2001). In the case of Neptune, a new model based on the LWS data has been adopted (Orton et al. 2000). LWS was able to observe some stellar calibrators (Lim et al. 1997), although these observations were difficult to make due to poor signal-to-noise in the relatively narrow LWS bandwidth. However, the stellar spectra did demonstrate a consistency with the Uranus-Mars framework, in the LWS 45–170 μm region. In this paper we present the totality of results from the ISO LWS spectra obtained on α Boo and α Tau.

The long-wavelength stellar spectral extrapolations are based upon the assumption that these calibrator stars are not attended by extensive chromospheres. Radiometric testing with ISOPHOT suggests (Muller & Lagerros 1998; Schulz et al. 2001) that these extrapolations were meaningful, i.e. consistent with calibrations based on asteroids and planets. It would be of great interest, both scientific and pragmatic, to determine independently if these same stellar calibrators radiate as predicted in the millimeter domain. The basis for mm-wave absolute flux calibration is Mars. Therefore, we observed the stellar calibrators against Mars, or against secondary microwave standards that were ultimately traceable to a comparison with Mars, Uranus, or Neptune. By this means we hoped to provide a link between the reference flux density scales of planets and stars and to unify flux calibration across the infrared-millimeter regime. Early efforts in this direction at Berkeley were described by Wrixon et al. (1971), and Welch & Gibson (2001) are continuing the radio absolute calibration work.

2. The observations

Table 1 summarizes our various sets of millimeter observations, indicating the array configurations and frequencies used, the times dedicated to actual integrations on the stars themselves, the phase and flux calibrators (chosen to be as close to each star's direction in the sky as possible), and the primary or secondary mm-calibrator observed with each set of stellar observations. A few measurements were taken in the B-array, with which planetary calibrators like Mars were partially resolved, necessitating an extra step in the calibration process to calculate the flux expected on the shortest baseline pairs (see below). Consequently, we preferred measurements in C- or D-array configurations. Angular diameters of these stars from optical to mid-infrared regions are of order 20 mas, rendering them unresolved targets in all these configurations, as were the local calibrators chosen. On the basis of estimates of the BIMA performance at 1 and 3 mm, our observing scripts called for typical tracks of several hours' duration, of which between roughly 2 and 4 hours were spent on the stars themselves.

This was a continuum experiment, and we selected observing frequencies from considerations of the expected stellar spectra, receiver performance, and atmospheric transmission. Whenever possible we included measurements of Mars with each set of stellar and local calibration source observations, in an attempt to unify the methods for calibration. For those few data sets taken in an array configuration that resolved Mars, we calculated visibilities as a function of baseline (in kiloλ) and applied these partial-resolution factors to the Mars model (Wright 1976) flux densities using our shortest baseline pairs.

Sometimes no planet was visible close in time to our observing tracks. We then resorted to MWC 349 when it was available because Hat Creek has a long series of observations of this star, it is relatively bright, has shown no statistically significant variability in our archives, and has been modeled in detail by Dreher & Welch (1983) so that flux extra/interpolation to our frequencies is viable. For our final observations, in December 2000, we used W3OH as reference for our α Tau track, again because of its relative proximity to this star, long-term temporal stability of signal, and the available multifrequency Hat Creek archives which enable us to interpolate between its known flux densities at other frequencies to our own, by treating it as having a canonical HII region spectrum and including the frequency dependence of the Gaunt factor. Other secondary references such as 1415+133 and 0530+135 were likewise observed when no other obvious flux reference presented itself. Independent observations of these were extracted from the Hat Creek archives, preferably with respect to a primary or acceptable secondary standard. In such circumstances, Table 1 carries the primary standard to which the flux pedigree of such a secondary is traceable.

Upper and lower sidebands were processed independently, maps made of the stars at each frequency, and peak flux densities extracted (see the final column of Table 1). Sometimes, weather condition were adequate in the lower sideband but led to unacceptably large noise in the upper sideband. In such cases we eliminated the noisy datasets which were readily recognized by the presence of artifacts, such as global striping, or large, negative-going blobs, in the maps. To estimate the uncertainties in the tabulated peak flux densities derived from any map, we used the standard deviation calculated from substantial regions of the map that excluded the target star itself. To combine the simultaneous upper and lower sideband maps at one epoch, we used inverse-variance weighting of the two maps based upon these noise estimators, relying upon the MIRIAD task MATHS. Likewise, we combined results across epochs.

3. Self-calibration of the 1-mm data

Phase calibration of interferometer data relies on transferring phases accurately from a point source (usually a QSO) to the target source. The accuracy of the calibration depends on the distance between source and calibrator, baseline errors, atmospheric phase stability, and the signal-to-noise ratio (SNR) in the phase measurement of the calibrator. All sources of phase error result in decorrelation of the calibrated image; i.e., a lower amplitude in the final map compared with perfectly calibrated data. Self-calibration offers a way to eliminate these phase errors, but is limited by the timescale on which phase can be accurately measured on the target source itself.

In the case of α Boo, the measured peak flux density in the normally calibrated image is about 50 mJy. Given the system temperature (350K), bandwidth (670 MHz, reduced from 800 MHz due to edge-channel flagging in the wideband average), and a correlator efficiency of 0.88 (2-bit) for these observations, the expected noise in a single-interferometer measurement is about 70 mJy in 10 min. Using self-calibration with a 9-element array improves the SNR for antenna-based phases by about a factor of 3, due to baseline averaging. The expected r.m.s. noise in the antenna-based phases using self-calibration is, therefore, about 25 mJy in 10 min. Assuming the true flux of α Boo to be 80 mJy, we would expect an SNR of about 3 using 10-min averaging on the source. The expected phase error for an SNR of 3 is $\sim 20°$ for each antenna (arcsin(1/3)). The decorrelation expected for an r.m.s. phase error of 20° is about 6% (reduced amplitude = $\exp(-r^2/2)$, where r=the r.m.s. phase error in radians). It would, therefore, appear safe to use an interval of 10 min or longer to self-calibrate the 1-mm α Boo data in phase. Of course, any additional phase error (e.g., atmospheric) incurred during the self-calibration interval will increase the decorrelation in the final image.

We can estimate the amount of atmospheric decorrelation expected. The average r.m.s. delay path in 10 min for a 100m baseline on the day of the α Boo 1-mm observations (01 Jun 2000) was 210 μm, or ~1 rad at 1360 μm wavelength. In D-array, the maximum baseline is about 30m. Assuming that the atmospheric r.m.s. phase scales as $(\text{baseline})^{5/6}$, the r.m.s. phase becomes 0.37 rad on the longest baseline $[(30\text{m}/100\text{m})^{5/6} * 1 \text{ rad}]$, and about 0.2 rad for the median baseline of 15m. The expected atmospheric decorrelation in 10 min for the 30m baseline (r=0.37 rad) is 0.85, and for the 15m baseline (r=0. 2rad) is 0.98. Thus, atmospheric decorrelation on 10-min timescales is not expected to be very important, and phase variations on the longer timescales will be removed by the self-calibration.

We validated these ideas on the June 2000 observations of α Boo by experimenting with self-calibration timescales in the reduction of the lower side-band data. The total cleaned flux in the resulting images of this star showed a spread of only 3.5%, while the more relevant quantity, the stellar peak flux densities, were 82.1, 81.5, and 81.1 mJy for a 15-, 20-, and 30-min timescale. We settled on a 20-min self-calibration timescale to reduce the data for α Boo, and 30 min for α Tau.

The final rows in Table 1 present the combined peak flux density information based on the totality of the available, good quality, stellar data for α Tau and α Boo. The corresponding images from which these final flux densities were determined appear as Figure 1.

4. Observations with LWS on ISO

LWS made two AOT observations of α Boo in revolutions 448 and 608. Both observations consisted of 6 forward and 6 backward scans, taken with an oversampling of 4. There were four observations of α Tau, two made in revolution 818, and one each in revolutions 848 and 861. The observations of α Tau each consisted of 28 scans, 14 in each direction with an oversampling of 4.

The LWS data were processed with Offline Processing version 10 and all the data were reduced using the Infrared Spectral Analysis Package (ISAP). The reduction steps consisted of removing outliers and averaging over individual detectors at maximum resolution, clipping at 2.5σ. No attempt was made to scale the detectors to make the sub-spectra overlap although we accomplished this outside ISAP using the splicing techniques described by Cohen et al. (1992b) for constructing absolutely calibrated spectra. As care was taken to use the same number of scans in each direction, the effects due to transients in the data are minimal and no transient correction was applied.

The fundamental Uranus model for calibrating the LWS is a synthesis of globally averaged Voyager Infrared Interferometer Spectrometer (IRIS) data up to 50 μm and James Clerk Maxwell Telescope (JCMT) data covering the 0.35–2 mm wavelength range (Griffin & Orton 1993) with a radiative transfer model similar to the one described by Griffin & Orton (1993).

Figures 2 and 3 illustrate these reduced LWS spectra for each star by presenting the mean spectrum, with the $\pm 3\sigma$ bounds for α Tau (which has more LWS data and higher signal-to-noise) and $\pm 2\sigma$ bounds for α Boo (with its noisier data sets). The sizeable triangular excursions in the two spectra near 53 and 106 μm represent our inability, for objects as faint as these normal stars, to remove the effects of the substantial leaks of 1.6-μm radiation to which LWS is prone. We have cleaned the observed spectra by 30-point boxcar smoothing the data (equivalent to about a 2 μm interval); α Tau's combined spectrum contained 1181 wavelength points, α Boo's 706 points. Each figure incorporates the absolutely calibrated model continuum spectra that we have computed (see below) as the almost flat long-dashed lines that cross the figures, and the mean$\pm 1\sigma$ bounds on our older calibrated energy distributions (dash-triple-dotted lines) delivered to ISOPHOT in January 1996.

Note that the new, more specific, calculations of stellar continuum spectra fall well within the uncertainties associated with the calibrated spectra originally delivered to ISO. We wish to quantify the degree of accord between measured and modeled spectra in the far-infrared for each star. The grating simultaneously illuminated the ten LWS detectors, and each detector was wavelength and flux calibrated separately. Therefore, LWS consists of ten spectrally independent detectors. The degree of oversampling of these stellar spectra was 4; consequently, adjacent points in Figures 2 and 3 are not independent. Therefore, to quantify the consistency of observations and predictions, and to handle the dependence of adjacent LWS points in the fully-plotted spectra correctly, we offer Figures 4 and 5. These represent the inverse-variance weighted average of all the meaningful data in each of the separate LWS detectors (i.e. after the rejection of data caused by the H-band leaks), and the associated 1σ uncertainties. Ordinates are plotted in terms of the ratio of observed to predicted flux densities in each independent wavelength block, versus wavelength, to highlight the deviations from the new spectral energy distributions. Abscissae represent the actual wavelength ranges usable for each star in each detector, plotted at the average wavelength for each detector.

All the separate detectors lie within 2σ of the newly modeled energy distribution for each star. We deduce that the underpinning Uranus calibration of LWS, the totally independently calibrated stellar spectra made by our older model extrapolations of the empirical 1.2–35 μm spectra, and the newly calculated, absolutely calibrated, emergent stellar energy distributions are all in good agreement. If we further average the results for the independent detectors for each star with inverse-variance weighting we can assert quantitatively that, for α Tau, this mean scale factor is 1.000 ± 0.011 (over nine detectors) while, for α Boo, the factor is 1.012 ± 0.025 (over seven detectors). Therefore, empirical stellar and planetary calibrations used by ISO, and state-of-the-art modeling, are absolutely reconciled to 3.3% (3σ) for the better observed α Tau, and 7.5% (3σ) for the more poorly observed α Boo.

5. The Radiative Equilibrium Model Atmospheres

5.1. Atmospheric parameters and computation of the emergent spectrum

The spectrum calculations were carried out with the SOURCE model atmosphere program in essentially the same fashion as described in Carbon et al. (1982). Specifics pertinent to the current calculations are described in this section, while a complete discussion may be found in Carbon et al. (2002).

For α Tau, we adopted an effective temperature of 3920 K (Blackwell et al. 1991) and a log(g) of 1.5 (Smith & Lambert 1990). For the isotopic abundances of C, N and O, we adopted $\log \epsilon(\mathrm{C}) = 8.40$, $\log \epsilon(\mathrm{N}) = 8.20$, $\log \epsilon(\mathrm{O}) = 8.78$, ${}^{12}\mathrm{C}/{}^{13}\mathrm{C} = 10$, ${}^{16}\mathrm{O}/{}^{17}\mathrm{O} = 562$, and ${}^{16}\mathrm{O}/{}^{18}\mathrm{O} = 475$ (Harris & Lambert 1984; Smith & Lambert 1990). The remaining metal abundances were chosen to be solar, following the lead of Smith & Lambert (1985). As discussed in Carbon et al. (2002), these choices are entirely consistent with current determinations of the parameters of α Tau. Bertrand Plez (Plez 1999) kindly computed an α Tau model atmosphere for us done in the plane parallel approximation using the aforementioned parameters and the programs described in Plez et al. (1992). This model structure is tabulated in Carbon et al. (2002). For α Boo, we adopted a slightly revised version (Peterson (1995): hereafter PDK) of the Peterson et al. (1993) model atmosphere which has more depths than the original. This atmosphere has an effective temperature of 4300 K, log(g) of 1.5, [Fe/H] = -0.5, and other elemental abundances as determined by Peterson et al. (1993). The column mass (g cm^{-2}) *vs.* temperature relations for both the PDK α Boo and Plez α Tau models were linearly extrapolated to shallower depths as required to obtain optical transparency at the longest wavelengths. For the PDK α Boo model, the extrapolated layers are shallower than 0.010 g cm^{-2}; for the Plez α Tau model, shallower than 0.020 g cm^{-2}. The resultant model atmospheres are shown in Figure 6.

It should be stressed that both of the above adopted model atmospheres have purely radiative equilibrium surface temperature structures. Specifically, they do *not* have chromospheric temperature rises, a point whose importance will become evident later. We have included in Figure 6, for comparison, the Ayres & Linsky (1975) (AL) α Boo chromospheric model and the Kelch et al. (1978) (KEL) α Tau chromospheric model B. These chromospheric models are semiempirical, derived from non-LTE analyses of Ca II and Mg II line fluxes. While these chromospheric models are now over 20 years old, they are very similar from the upper photosphere, through the temperature minimum region, and into the lower chromosphere to models of α Boo and α Tau used by Wiedemann et al. (1994), and the α Tau model derived by McMurry (1999).

Using the Plez α Tau atmosphere and parameters detailed above, we have computed the synthetic spectrum for α Tau over the entire LWS range, 43 to 197 μm. The spectrum was computed using a full set of molecular line opacities which includes all the principal isotopomers of CO, SiO, OH, CN, and H_2O and using a wavelength mesh which provided $\approx$2.5 points per Doppler width. To allow comparison with the LWS observations, we convolved the high-resolution result with a Gaussian instrumental profile function having a FWHM equal to 0.29 μm for $\lambda \leq 90.5$ μm, and 0.60 μm, $\lambda > 90.5$ μm (e.g., Gry et al. (2000)). A detailed description of this spectrum may be found in Carbon et al. (2002). *At the ISO LWS and the BIMA spectral resolutions* all differences between the pure continuum and the synthetic spectrum computed with the full set of molecular line opacities are less than 2%; beyond 100 μm, they are less than 1%. This is *much less* than the noise level in the observed α Tau spectra in this region. As a consequence, there is no advantage gained in using the full synthetic spectrum. For clarity we will use only the continuous spectrum in our comparisons with the α Tau observations. Since precisely the same situation occurs in the case of α Boo, we shall use the continuum alone for comparisons there as well.

5.2. Depth of formation and brightness temperatures

For both the PDK α Boo and the Plez α Tau models, the dominant continuous opacity in the continuum-forming layers for wavelengths redward of the H^- opacity minimum at 1.64 μm arises from H^- free-free. This opacity increases in strength as λ^2. As a result, the emergent continuum flux is formed at progressively shallower layers in the stellar atmosphere as one proceeds to longer wavelengths. Figure 6 illustrates this point for the Plez α Tau and the PDK α Boo models. In this figure we have marked, for the radiative equilibrium models, the atmospheric depths for which the continuum optical depth, τ_λ^c, reaches unity at the indicated wavelengths. That is, we have marked the column masses at which $\tau_\lambda^c = 1.0$; roughly speaking, depths near this value make the greatest contribution to the emergent continuum flux at wavelength λ. Note, for example, that the continuum fluxes between 1 mm and 3 mm are sampling very different parts of the atmospheric temperature structure in both radiative equilibrium models than, say, the continuum fluxes at 2.3 μm. Indeed, the longest wavelengths are sampling, *in the continuum*, atmospheric levels reached only at the cores of lines in bluer portions of the spectrum. Only when one proceeds to the vacuum ultraviolet and its strong photoionization continua of metals is it possible to reach in the continuum the shallow atmospheric levels probed by the continuum at long wavelengths (e.g. Figure 1 of Vernazza et al. (1976)). Thus, the far-infrared continuum is an effective probe of the shallowest stellar layers which can supplement the information derived from line cores and UV continua.

As noted above, there is very little difference between the full synthetic spectrum and the spectrum of the continuum. Figure 6 provides an important clue as to why spectral lines generally become less prominent at longer wavelengths. It is evident that, as one goes to shallower depths in the models, the slope of the temperature-column mass relation becomes smaller. The significance of this can be appreciated by considering an absorption line in the α Tau model with a characteristic, depth-independent, line core/continuum opacity ratio of 1000. If the absorption line occurs at a wavelength of 2.3 μm, the continuum will be formed at $\approx$5200 K and the line core will be formed at $\approx$3200 K. The same line at a wavelength of 200 μm will have the continuum formed at $\approx$3100 K and the line core at $\approx$2600 K, a much smaller temperature difference between line core and continuum than at 2.3 μm. Couple this with the decreasing temperature sensitivity of the Planck function as one goes to longer wavelengths and one has a recipe for progressively less prominent spectral features.

Figure 7 provides another window into the wavelength dependence of continuum formation. In the upper panel of Figure 7 we show the column masses for which $\tau^c_\lambda = 1.0$ over the spectral range 0.5 μm to 200 μm. As noted above, there is a steady march to progressively shallower depths of continuum formation as one goes to longer wavelengths. Since the dominant H$^-$ bound-free opacity peaks at roughly 0.825 μm, continuum fluxes at wavelengths between 0.825 μm and 1.64 μm probe the same atmospheric layers as continuum fluxes between 1.64 μm and 6.5 μm. Longward of 6.5 μm, the continuum flux probes atmospheric layers accessible only in line cores and in the metal bound-free continua of the vacuum ultraviolet.

In the lower panel of Figure 7 we show the continuum "brightness temperature" over the same spectral range for both models. The brightness temperature is defined here as the temperature of a blackbody which gives the same flux as the model atmosphere at the indicated wavelength. Three points are important. First, neither α Boo nor α Tau could have its continuum fluxes over any large spectral range matched by a blackbody of a single temperature. Second, the blackbody temperatures which do match the model fluxes at specific wavelengths are generally quite different than the effective temperatures of the models (or the stars) themselves. Third, comparing with Figure 6, one sees that the brightness temperature is different than $T(\tau^c_\lambda = 1.0)$, the temperature of the atmospheric layer at which optical depth unity is reached in the continuum at wavelength λ. This occurs because the emergent flux actually represents a weighted integral of the source function over depth rather than the conditions at any specific depth. In the particular cases of the PDK and Plez models, $T(\tau^c_\lambda = 1.0)$ is systematically larger than the brightness temperature at the same wavelength over the spectral range shown in Figure 7. The differences between $T(\tau^c_\lambda = 1.0)$ and brightness temperature vary systematically with wavelength. The differences are greatest at 1.64 μm and decrease to the red. *Beyond 40 μm, the differences are always less than 100 K.* For this reason, the brightness temperature is a good first guess at $T(\tau^c_\lambda = 1.0)$ at the longer wavelengths. We will make use of this result later when we discuss the brightness temperatures implied by the observations.

6. Discussion

6.1. Comparison of fully modeled and Engelke continua

To convert the model surface fluxes to predicted fluxes at the Earth, we have adopted the angular diameter, 21.0±0.2 mas, of Quirrenbach et al. (1996) for α Boo (measured by optical intensity interferometry) and the angular diameter, 20.88±0.10 mas, of Ridgway et al. (1982) (using lunar occultation) for α Tau. Cohen et al. (1996b) presented a comparison of a generic red-giant continuum calculation relevant to α Tau and the approximation to the stellar continuum described by Engelke (1992), based on the assumed dominance of H^- free-free opacity in cool giants. Figures 8 and 9 provide these same comparisons with our newly calculated spectra, specific to the fundamental parameters of α Tau and α Boo. The Engelke functions displayed in these figures serve as adequate ($\sim$5% level) continuum approximations from 10–200 μm (1.9% maximum deviation for α Boo; 4.8% for α Tau). The deviations between Engelke approximations and our model energy distributions are too small to be discerned by ISO's Short Wavelength Spectrometer (SWS) given the real uncertainties associated with SWS Band4 (29.5–45 μm) observations, while the maximum deviations occur in the LWS range, where they are overwhelmed by the uncertainties associated with removal of the H-band leaks near 52 μm.

6.2. Evidence for the chromosphere at 1.4 mm and 2.8 mm

Table 2 shows the comparison between the observed fluxes and the predictions of the radiative equilibrium models. Only for the case of α Tau at 1.4 mm does there appear to be approximate agreement between the observed flux and the flux predicted from the radiative equilibrium model. The remainder of the observed fluxes are all significantly *larger* than the fluxes predicted by the models. The discrepancies are particularly striking in the case of α Boo.

We do not believe that the flux computation for the radiative equilibrium models could have errors sufficiently large to produce the marked differences between computed and observed millimeter fluxes. The model atmosphere code has been carefully vetted and the dominant continuous opacities are themselves quite well determined (e.g., van der Bliek, Gustafsson, & Eriksson (1996)). On the observational side, our derived errors for the observed 1.4-mm and 2.8-mm fluxes preclude dismissing the differences between observed and computed fluxes as simply due to measurement error. We believe other explanations must be considered.

Since the adopted angular diameters for these two stars appear to be extremely well determined, with standard deviations of $\approx$1% or less, they would not seem to be a significant source of error. Moreover, a major change in the angular diameters would compromise flux agreement for the $\lambda \leq 200$ μm region. Nevertheless, it should be noted that the Quirrenbach et al. (1996) diameter is an arithmetic mean of values measured from 0.45 μm to 2.2 μm and the Ridgway et al. (1982) diameter is a error-weighted mean biased toward values obtained at 1.6 μm and 3.8 μm. At any particular monochromatic wavelength, an observed angular diameter represents the apparent diameter of the $\tau_\lambda \approx 1.0$ surface of the star. Since, as shown in Figures 6 and 7, there is a progressive march in depth of continuum formation to ever shallower atmospheric layers as one moves redward of 1.64 μm, the angular diameters themselves should increase with wavelength. If the angular diameters at 1.4 mm and 2.8 mm are substantially larger than those at the wavelengths of the Quirrenbach et al. (1996) and Ridgway et al. (1982) observations, our predicted fluxes in Table 2 could be seriously underestimated. We can roughly estimate the magnitude of this source of error, at least in the case of the radiative equilibrium models. In Table 3 we show the physical radii of α Boo and α Tau based on the indicated angular diameters and

Hipparcos parallaxes (ESA 1997). We also show the physical distances in the radiative equilibrium models between $\tau^c_{1.64\mu m} = 1.0$ and $\tau^c_{2.8mm} = 1.0$.

Given the tabulated numbers, it is clear that, for the PDK and Plez models, the atmospheric extent in the continuum at 2.8 mm is not sufficient to seriously affect our predicted fluxes. We find a similar result in the case of the only model chromosphere with a published height scale, McMurry's chromospheric model for α Tau (McMurry 1999). The McMurry atmosphere is plane-parallel and hydrostatic, constructed with log g = 1.25. Note that this gravity leads to a more distended atmosphere than does the higher gravity we adopted. The McMurry atmosphere has an extent of $\approx 2.6 \times 10^{11}$ cm between the layers where the 1.64 μm continuum is formed and the layer with T = 7120 K in the chromosphere. This extent is only 8% of the stellar radius and again seems too small to explain the discrepancy between computed and observed fluxes. Finally, as we will describe in Section 6.6, Drake & Linsky (1986) determined that α Boo has essentially the photospheric radius at 2 cm. Given the expected increase in angular diameter with wavelength, this would imply that α Boo would have the photospheric radius at ¡ 2 cm as well.

We believe that the flux excesses at 1.4 mm and 2.8 mm are signatures of the chromospheric temperature rise in the two red giants. Unfortunately, accurate computation of the 1.4-mm and 2.8-mm fluxes and depths of formation for chromospheric models is well beyond the current study. Such a computation would require a non-LTE treatment of the H ionization equilibrium and perhaps also of the ionization equilibria of the principal metallic electron donors in the layers near the temperature minimum where H is not yet the principal source of electrons. Without non-LTE values for the neutral H, proton and electron concentrations which determine the dominating H and H^- free-free opacities at 1.4

and 2.8 mm in the lower chromospheres, we cannot be certain just where $\tau_\lambda^c = 1.0$ might occur in the chromospheric models.

Nevertheless, we feel there is significant circumstantial evidence that stellar chromospheres could explain the flux excesses. This circumstantial evidence comes from the depths at which $\tau_\lambda^c = 1.0$ in Figure 6. In the case of the Plez α Tau model, $\tau_{1.4mm}^c = 1.0$ occurs significantly deeper than the point where the KEL α Tau chromospheric model begins its temperature rise. Since the chromospheric and radiative equilibrium models have essentially the same temperatures near this point, it is not surprising that they would yield similar emergent fluxes, just as Table 2 indicates. The $\tau_{2.8mm}^c = 1.0$ point occurs in the Plez model only slightly deeper than the depth where the KEL model starts its chromospheric rise. Since the observed flux at 2.8 mm is markedly brighter than predicted by the Plez model, this may be an indication that the α Tau chromosphere begins its temperature rise slightly deeper in the atmosphere than where Kelch et al. (1978) placed it. Alternatively, the discrepancy may arise because the optical depths in the chromosphere are significantly larger than those in the Plez model near the temperature rise. At least in the LTE case, the higher temperatures of the lower chromospheric layers will produce greater opacity through increased electron concentrations. These higher opacities will cause $\tau_{2.8mm}^c = 1.0$ to occur at shallower depths in the KEL chromospheric model than in the case of the substantially cooler Plez radiative equilibrium model. Such an opacity increase could cause the 2.8 mm depth of formation to be pushed substantially shallower (i.e., hotter in the KEL model) than the temperature minimum in α Tau, consistent with the higher observed fluxes in Table 2. The same arguments are even more compelling in the case of α Boo. Here, since the chromospheric rise occurs relatively deeper than in α Tau, both the 1.4 mm and the 2.8 mm points of the PDK radiative equilibrium model lie well *above* (i.e., shallower than) the temperature minimum of the AL model. Thus, it is not surprising that the PDK model significantly underpredicts the flux at both 1.4 mm and 2.8 mm in α Boo.

We show in Table 2 the brightness temperatures corresponding to the observed fluxes and cited angular diameters as well as the brightness temperatures predicted by the PDK and Plez models. The error estimates of the brightness temperatures were computed considering *only* the errors in the observed fluxes. Comparing the observed brightness temperatures with the electron temperatures in the AL and KEL single-component models (e.g., Figure 6) does not immediately suggest a glaring discrepancy. This is the coarsest of comparisons, however, devoid of any information regarding the depth of formation of the chromospheric continuum. A quantitative comparison between the AL and KEL chromospheric models and our observed millimeter fluxes requires at least non-LTE modeling of the relevant ionization equilibria. As we shall note below, producing the observed fluxes may require dealing with multi-component, extended atmospheres as well. There is one point to be considered by future observers and modelers. We draw attention to the insignificant difference between the brightness temperatures at 1.4 mm and 2.8 mm in α Boo. These are our most accurate measurements and seem to indicate little change in temperature between the atmospheric levels where these fluxes are produced. It will be very interesting to learn whether this result actually agrees with non-LTE flux predictions based on the continuously rising Ayres & Linsky (1975) chromospheric model, or whether the observations in fact require a flattened temperature profile at the relevant depths.

6.3. The transition from photosphere to chromosphere

We would like to again emphasize the importance of the spectral region from $\approx$30 μm to several millimeters. Fluxes from this spectral region are essentially a map of the mean time- and spatial-averaged temperature structure of the upper photosphere and chromosphere for stars like those we consider here (see Figure 6). Accurate fluxes measured through this spectral region allow us to test directly model temperature structures over the very interesting depth range in which non-radiative processes like shocks begin to alter the mean structure. By selectively sampling progressively longer wavelengths, we can follow the important transition from photosphere to chromosphere, locating the depth at which purely radiative models like the PDK and Plez models begin to fail.

Considering Figures 5 and 11, we see that for α Boo the chromospheric transition occurs somewhere between $\approx$125 μm and 1.4 mm. Given this rather uncertain location, it seems inadvisable to use either radiative equilibrium models or Engelke functions to represent α Boo for calibration purposes anywhere beyond 125 μm. In the context of the PDK model (see Figure 7), this uncertainty in the wavelength of the transition from photosphere to chromosphere corresponds to nearly an order of magnitude in column mass, between 5.3 and 0.68 gm cm^{-2}. Ayres & Linsky (1975) placed the temperature minimum in α Boo at 1.8 gm cm^{-2}, nicely within our range.

For α Tau, considering Figures 4 and 10, we see that an argument may be made for the transition to the chromosphere occurring between 1.4 mm and 2.8 mm. This corresponds to only a factor two in column mass in the Plez model, spanning 1.0 to 0.5 gm cm^{-2}. This is only slightly deeper than the estimate of the temperature minimum of α Tau at 0.3 gm cm^{-2} made by Kelch et al. (1978). However, the flux point at 1.4 mm in α Tau is our lowest S/N measurement. For another estimate of the α Tau temperature minimum location, we can consider the somewhat higher S/N measurement at 1.2 mm reported by Altenhoff et al. (1994). This measurement and additional observations by other observers at cm wavelengths are discussed later in Sections 6.5 and 6.6. We direct the reader's attention to Figure 15 where we display all the observations of α Tau discussed in this paper as brightness temperatures. If we ignore our low S/N point at 1.4 mm, an argument can also be made, using the remaining long wavelength points, for a transition to the chromosphere near $\approx$900 μm. This corresponds to a column mass of $\approx$1.5 gm cm^{-2}, significantly deeper than the Kelch et al. (1978) value of 0.3 gm cm^{-2}. Given the uncertainty of the 1.4 mm point, it is not possible to resolve this issue with the available data.

For α Boo, our continuum-based results for the location of the chromospheric rise are consistent with the results obtained from detailed non-LTE analyses of strong atomic lines. In the case of α Tau, one reading of the available data yields a result close to the location deduced from the detailed line analyses, while another suggests a chromospheric rise beginning significantly deeper in the atmosphere. This uncertainty can be resolved with better observations. Indeed, it will be invaluable to have a finer wavelength mesh of even better determined fluxes throughout the far-infrared, sub-mm, and mm domains for both α Boo and α Tau. *Nevertheless, it is clear from the available data that long wavelength flux measurements are a powerful tool for probing the temperature minimum region.*

6.4. Implications for Simple Two-Component Chromospheric Models

Work on stellar chromospheres has been largely devoted to constructing single component, time-independent, plane-parallel models which reproduce the cores and wings of strong visible and UV atomic lines (e.g., Kelch et al. (1978), Ayres & Linsky (1975)). In the cases of α Boo and α Tau, strong evidence for multi-component chromospheres has come from observations of the infrared CO vibrational-rotational fundamental lines (e.g., Heasley et al. (1978), Wiedemann et al. (1994)) and the ultraviolet CO Fourth Positive System electronic lines (McMurry & Jordan 2000). Wiedemann et al. (1994) proposed a simple two-component "bifurcation model" stellar chromosphere "...with physically distinct areas of hot and cool material at the same altitude...". In this model, the CO fundamental lines are produced by a cool component very similar in temperature structure to the Plez and PDK radiative equilibrium photospheres. This cool component must occupy all but a few percent of the visible stellar disk in order to reproduce the CO observations. The remaining small portion of the stellar disk is covered by a hot component similar to the AL and KEL chromospheric models of Figure 6. This hot component supplies the atomic line fluxes at short wavelengths, which were the principal chromospheric diagnostics, while making no appreciable contribution to the 5 μm CO spectrum. Since the original one-component chromospheric models (e.g., AL and KEL) were full-disk models, the temperatures in each layer of the hot component of the bifurcation model must be appropriately increased to compensate for the greatly reduced area. For α Boo, Wiedemann et al. (1994) attempted to estimate just how much hotter the layers would have to be for the specific problem of reproducing the Ca II K line profile when the cool component covered 90% of the stellar disk and the hot component 10%. They found that a temperature increase of "...only a few hundred degrees..." sufficed. This comparatively modest increase was possible because of the exponential temperature dependence of the Planck function at shorter wavelengths.

Our millimeter observations provide a chance to test the Wiedemann et al. bifurcation model in a wavelength range where the temperature dependence of the Planck function for *both* components is linear. In this model, the net observed flux, $S_{obs}(\lambda)$, is related to the flux contributions from the hot component, $S_h(\lambda)$, and the cool component, $S_c(\lambda)$, as:

$$S_{obs}(\lambda) = f_c\, S_c(\lambda) + (1 - f_c)\, S_h(\lambda)$$

where f_c is the fraction of the stellar disk covered by the cool component, and $(1 - f_c)$ is the fraction covered by the hot component. If we substitute our observed millimeter fluxes for $S_{obs}(\lambda)$ and the fluxes predicted by the PDK and Plez models for the cool component fluxes, we can determine the required hot component fluxes for a given f_c. In Table 4 we show the hot component fluxes which result when one lets $f_c = 0.90$, the coverage fraction chosen by Wiedemann et al. for their α Boo example. For $S_{obs}(\lambda)$ and $S_c(\lambda)$ we used appropriate values from Table 2. Since no chromospheric component was required for α Tau at 1.4 mm, we derived no hot component flux for that case.

To better discuss the deduced hot component fluxes, we have indicated in Table 4 the brightness temperatures, $T_B(\lambda)$, which correspond to the observed, cool, and hot component fluxes. These were computed by assuming that the flux can be represented as coming from a spherical blackbody of angular diameter, α, and temperature, $T_B(\lambda)$. In the long wavelength (Rayleigh-Jeans) limit, $T_B(\lambda)$ is related (e.g., Drake & Linsky (1986)) to the observed flux, $S_{mJy}(\lambda)$, from such a blackbody as:

$$T_B(\lambda) = \frac{(1.763 \times 10^9)\, S_{mJy}(\lambda)}{\alpha^2\, \nu_{GHz}^2}$$

where $S_{mJy}(\lambda)$ is in mJy, α is in mas taken from Table 3, ν_{GHz} is the frequency in GHz, and $T_B(\lambda)$ is in kelvins.

It is immediately clear on inspecting Table 4 that a simple bifurcation model with $f_c = 0.90$ leads to very high brightness temperatures for the hot component. These brightness temperatures are higher than the electron temperatures of the very highest and hottest chromospheric layers in the AL and KEL models. Indeed, they are more like the electron temperatures found in the transition region (McMurry (1999)) above the chromosphere. Based on Figure 6 one naively might have expected brightness temperatures below 10000 K, more characteristic of the electron temperatures in the layers just above the temperature minimum. Indeed, as we noted above, the observed brightness temperatures do seem roughly compatible with the standard full-disk chromospheric models. It should be noted that larger values of f_c, considered by Wiedemann et al., would lead to even higher brightness temperatures for the hot component than computed here. Unless non-LTE effects can provide for the discrepancies, it appears that the AL and KEL chromospheric models cannot yield high enough brightness temperatures when used in the bifurcation model without first dramatically increasing their temperatures in the 1.4 mm and 2.8 mm continuum-forming layers. A temperature increase of "...only a few hundred degrees..."

would seem quite inadequate. Detailed computations, well beyond the scope of this investigation, will be required to resolve this particular issue satisfactorily.

It may well be that the simple thermal bifurcation model is insufficient for reproducing the CO fundamental vibration-rotation line cores *and* the millimeter continuum fluxes we report here. Evidence for time-dependence of chromospheric coverage, temperature, and/or structure has been found by O'Brien & Lambert (1979, 1986) in observations of the He I 10830 line variations and by Robinson et al. (1998) in UV continuum and emission line variations. Carpenter et al. (1985) deduced substantial chromospheric extents for α Boo and α Tau based on observations of the C II UV 0.01 multiplet. Based on UV CO and atomic line emission/absorption, Ayres et al (1997) and McMurry & Jordan (2000) argue for complex structures within the stellar chromospheres. Collectively, the stellar studies and high spatial and temporal resolution work in the solar case (e.g., Ayres, Testerman & Brault (1986), Ayres & Rabin (1996), Uitenbroek (2000a,b)) indicate that a single component, time-independent, plane-parallel chromosphere is not adequate and that something rather more sophisticated is required. It is our hope that submillimeter and millimeter continuum observations, which sample the upper photosphere and lower chromosphere, can prove useful in the effort to constrain these more sophisticated models.

Finally, before closing this section on the apparent disparity between our mm continuum measurements and the bifurcation model of Wiedemann et al. (1994), we wish to point out the following possibility for resolution. Wiedemann et al. were led to consider a two-component chromospheric model because of the need to reconcile the non-LTE atomic lines and the essentially LTE CO fundamental line cores. As indicated in the references cited above, much the same conflict exists in the solar case, although greatly magnified by the ability to observe spatial and temporal detail. In the solar case, as in the stellar, the CO fundamental line cores indicate lower temperatures than derived from other indicators of shallow layer temperatures like strong atomic lines, UV continua, and far-infrared continua. Uitenbroek (2000a,b) suggests that the lower atmospheric temperatures deduced from the CO fundamental line cores in the sun may be a result of the CO not being in instantaneous chemical equilibrium, the usual approximation used in computing CO molecular concentrations. Uitenbroek cites the long CO association times in the upper solar atmosphere reported by Avrett et al. (1996) as part of the support for this hypothesis. Given the much lower gas pressures in the temperature minimum regions of red giants ($\approx$60 dynes cm^{-2} for α Boo, $\approx$10 dynes cm^{-2} for α Tau) as compared with the sun ($\approx$1400 dynes cm^{-2}), it seems likely that Uitenbroek's suggestion regarding the CO may apply to the red giants as well. If so, then the CO formation is much more complex than modeled by Wiedemann et al. and the argument for a simple bifurcation model less compelling.

6.5. The mm-cm region

Figures 10 and 11 present our millimeter flux densities (filled circles) and the color-corrected IRAS measurements of each star at 12, 25, 60, and 100 μm (crosses). Each figure includes the PDK α Boo or Plez α Tau continuum spectrum, as appropriate, from 10 μm to 3 mm.

There are additional high-frequency radio continuum observations of these two K-giants in the literature. Altenhoff et al. (1986) made single-dish 86-GHz measurements of α Boo (21.4$\pm$7.5 mJy) with the IRAM 30-m telescope, while Altenhoff et al. (1994) likewise detected both α Tau and α Boo at 250 GHz, obtaining 51$\pm$6 and 78$\pm$8 mJy, respectively. There are also VLA centimeter measurements on both stars at 4.9, 8.4, and 14.9 GHz by Drake & Linsky (1986), and unpublished data by Drake, Linsky, & Judge from the compilation of radio data by Wendker (1995). These long wavelength measurements all have substantial uncertainties, in part due to the faintness of the stars, in part to the potential for confusion with extragalactic background objects. Nonetheless, in combination with our own radio data (Figures 10, 11) one sees that these high-frequency data (open diamonds) are in good agreement with our aperture synthesis measurements (filled circles).

In their study of radio emission from 39 cool giants and supergiants, Drake & Linsky (1986) were able to detect thermal emission at *both* 2 cm and 6 cm from three stars cooler than the Linsky-Haisch dividing line, α Boo (K2 IIIp), ρ Per (M4 II-III) and α^1 Her (M5 II). These three stars had spectral indices ($S_\nu \propto \nu^\alpha$) of $\sim$0.9 between 2 and 6 cm, compared with the canonical index of 0.60 predicted for an optically thick ionized wind with an inverse-square law density profile, or the index of 2.0 associated with a blackbody stellar disk. The intermediate index may stem from the 2 – 6 cm spectral range being a transitional region with a strong component of blackbody disk radiation at the low wavelength end and an increasing contribution from an ionized wind at the upper end. In this vein, Drake & Linsky (1986) found that the 2 cm radio emission of α Boo, α Tau, ρ Per, and α^1 Her could be interpreted as stellar disk emission with brightness temperatures of $\approx$ 10–15 $\times$ 10^3 K. As another point of reference, Reid & Menten (1997) detected six of their eight long period variables at 1.3, 2.0, and 3.5 cm, finding power laws for all six stars with slopes close to 2.0, indicative of optically thick blackbodies.

Given the above complex picture of longer wavelength radio continuum emission in cool evolved stars, it is interesting to briefly examine the frequency dependence of the radio emission in α Boo and α Tau which is *in excess of* that predicted by photospheric models. Figures 12 and 13 represent our spectra of the "excess" emission computed by subtracting out the flux contribution predicted by the PDK model for α Boo and the Plez model for α Tau. Note we have dropped our 1.4 mm α Tau point in constructing Figure 12 since it falls below the prediction of the Plez model. We find the non-photospheric flux components in each star to have slopes, F_λ, going as λ^{-3} to λ^{-4}; i.e. $S_\nu \propto \nu^1$ to ν^2. Clearly these bounds must be regarded cautiously since they depend upon the spectral intervals chosen. Limiting the wavelength range to 2 – 6 cm in α Boo, for example, would give the Drake & Linsky (1986) result of $\nu^{0.80}$.

6.6. Brightness temperatures for all the observed fluxes

It is valuable to convert the mm and cm fluxes from other observers into brightness temperatures and combine them with our data to gain an overview of the brightness temperatures over a broad spectral range. In Figures 14 and 15 we show the brightness temperatures corresponding to all the observed flux data between 43 μm and 6 cm used in our previous figures. For comparison we have also plotted the predictions of the radiative equilibrium models. In deriving brightness temperatures from the observed fluxes, we used the angular diameters of Table 3 in the following relation:

$$T_B(\lambda) = \frac{14387.75 \;/\; \lambda}{\ln(\,1\; + \;\frac{733.4090\,\alpha^2}{S_{Jy}(\lambda)\,\lambda^3})}$$

where $S_{Jy}(\lambda)$ is the observed flux in Jy, α is the angular diameter in mas, λ is the wavelength in microns, and $T_B(\lambda)$ is in kelvins. (We used the long wavelength limit of this exact expression earlier in Section 6.4.) The error bars in Figures 14 and 15 correspond *only* to the uncertainties in the observed fluxes. In the case of the α Tau data at 2 cm and 3.6 cm, no error values were reported by Wendker (1995) and we used our own rough estimates of the plausible errors.

The wavelength range of Figures 14 and 15 allows us to sample atmospheric depths which range from the upper photosphere on the low wavelength side, through the temperature minimum, and on into the chromosphere, and possibly higher, at the longest wavelengths. For both α Boo and α Tau, there is excellent agreement between the observed and predicted brightness temperatures for the IRAS and LWS wavelengths which sample the upper photospheres. From Figures 6 and 7 we see that the fluxes at these wavelengths arise from upper photospheric depths between roughly 25 and 6 g cm^{-2} column mass. In terms of a "standard" 1-μm continuum optical depth scale, these correspond to $\tau^c_{1.0\mu m} \approx 0.04 - 0.004$.

As we have noted in our earlier discussion of the fluxes (Section 6.3), the transition to the chromosphere clearly occurs somewhere beyond the reddest LWS wavelengths for both α Boo and α Tau. We also noted before the nearly constant brightness temperature between 1.4 mm and 2.8 mm in α Boo (Section 6.2). This constancy is especially interesting when seen now in the context of the other mm and cm fluxes. Clearly it will be very useful to fill in crucial wavelengths and reduce the uncertainties of some of the already observed wavelengths in both stars. Readers are strongly encouraged to compare these brightness temperature plots for α Boo and α Tau with the corresponding example for the solar case shown as Figure 4 in Vernazza et al. (1973). Figures 14 and 15 demonstrate that one can put useful constraints on the temperatures of upper photospheric and chromospheric layers with accurately observed long wavelength fluxes.

An important point needs to be emphasized regarding especially the longer wavelength points. The observed fluxes presumably come from progressively shallower stellar layers as λ increases. All of the brightness temperatures in Figures 14 and 15 have been deduced assuming the photospheric angular diameters of Table 3. As we noted earlier (Section 6.4), atmospheric extension may play a role in the chromospheric layers of α Boo and α Tau. Carpenter et al. (1985) estimated the extension of the chromospheres of these stars. They argued that the C II UV 0.01 lines which they studied were formed in chromospheric layers with temperatures of $\approx$8000 K in α Boo and $\approx$10000 K in α Tau. They deduced that these chromospheric layers had radii of $\approx 2.0\ R_*$ and $\approx 1.4\ R_*$, respectively, where R_* is the stellar photospheric radius. Although these estimates are, in the authors' words, "relatively crude", they do suggest that atmospheric extension may play a role at least in the hotter layers of the chromosphere. Different evidence of extension was found by Drake & Linsky (1986) in their study of 2 cm and 6 cm fluxes cited earlier (Section 6.5). In that study, they treated all the radio emission as coming from an optically thick ionized wind for which a "half-power radius" could be deduced. In the case of α Boo they found the 2 cm half-power radius was $\approx$R$_*$; at 6 cm, the half-power radius had grown to $\approx$1.7 R$_*$. Referring back to the long wavelength approximation for the brightness temperature (Section 6.4), we recall that, for a given observed flux, $T_B(\lambda) \propto 1/\alpha^2$, where α is the angular diameter. Since the shallowest layers may have angular diameters significantly larger than those of the photosphere, the corresponding brightness temperatures in Figures 14 and 15 should be regarded as upper limits. Clearly, detailed modeling which explicitly attempts to address this and other issues is required. Until such modeling is undertaken, it will be unclear which of the non-photospheric fluxes are best fit by a standard plane-parallel chromospheric model, a model chromosphere with atmospheric extension, or a model whose chromosphere blends into an ionized stellar wind, acting as a "radio photosphere" (Reid & Menten 1997; Drake & Linsky 1986).

6.7. Stellar absolute calibrators for ISOPHOT

Our original, theoretically extrapolated, continuum spectra for the two K-giants, supplied to ISOPHOT as absolutely calibrated energy distributions, are in extremely good agreement with our new calibrated synthetic spectra (Figures 2, 3), well within the ±6% uncertainties assigned to the original calibrators (Cohen et al. 1996b). The LWS spectra, reduced with respect to Uranus as calibrator, are consistent with the new (and old) synthetic spectra, thereby uniting far-infrared planetary and stellar calibrations at the few percent level (Figures 4, 5).

There are independent data on α Boo, derived from the validation of ISOPHOT's final pipeline (OLP10) (Richards 2001), that show it conforms to our 1996 model spectrum. In addition, Schulz (2001) has described the performance through the ISO mission of a significant number of ISOPHOT calibrators. By removing the contributions made by any particular source to the calibration process, and calibrating that source with respect to all other calibrators, one can assess the ratio of observed to modeled irradiance. Using the database described by Schulz (2001), which he has kindly made available to us, we have been able to extend the range over which our new model of α Boo can be tested, and to validate α Tau independently of our LWS data. For α Boo, we have determined the observed to modeled irradiance ratios for the ISOPHOT C120, C135, C160, C180, and C200 filters ("C" denotes the far-infrared camera within the ISOPHOT instrument, and each filter is designated by its reference wavelength in μm). Expressing these observed irradiance ratios with respect to our new modeled spectrum for α Boo we find: C100, 1.02±0.02; C120, 1.14±0.08; C135, 1.01±0.02; C160, 1.06±0.02; C180, 1.00±0.03; C200, 1.00±0.26. For α Tau, measurements are available solely in the C160 filter and yield a ratio of 0.96±0.05, with respect to our new model. We conclude that the independent absolute calibrations of LWS and ISOPHOT are in accord, and that our new models for these two stars describe the real stellar energy distributions essentially to the limits of these instruments ($\sim 200\mu$m).

7. Conclusions

Our first objective was to investigate the outer atmospheric structure in two normal K-giants through the comparison of observed and predicted far-infrared and microwave flux densities. We have found that for both α Boo and α Tau the radiative equilibrium temperature structures of the upper photospheres produce fluxes in agreement with the observations. For α Boo the agreement extends to at least 125 μm, corresponding to a column mass of $\approx$5.3 gm cm^{-2} in the atmosphere. For α Tau the upper photosphere produces agreement to at least 170 μm, corresponding to a column mass of $\approx$7.3 gm cm^{-2}. We have been able to put bounds on the location of the temperature minimum in α Boo based on far-infrared and mm continuum fluxes alone. These bounds are consistent with the value deduced from detailed non-LTE analyses of strong atomic lines. The location of the chromospheric rise based on continuum measurements in α Tau may either be slightly, or significantly, less than value deduced from strong atomic lines. More accurately determined mm fluxes, particularly at 1.4 mm, as well as observations in the sub-mm domain, will be crucial in settling this issue. Similarly, sub-mm observations will be of critical importance for α Boo since they will more closely pinpoint the location of the chromospheric rise in that star. The results indicate that our approach can be used to probe the upper photospheric and temperature minimum regions and can be applied with confidence to other red giants whose chromospheric lines have not been so thoroughly analyzed.

Our millimeter measurements strongly indicate fluxes arising from a stellar chromosphere. While we have not attempted a non-LTE analysis of these fluxes, some conclusions seem evident. First, the mm-fluxes appear to be compatible with single-component mean chromospheres like those of Ayres & Linsky (1975), Kelch et al. (1978), and McMurry (1999). Second, the observed mm-fluxes do not appear to be compatible with the Wiedemann et al. (1994) bifurcation chromospheric model, at least when current radiative equilibrium models are used for the "cold-component" and models like the AL and KEL are used for the "hot-component". We believe that this may be the first evidence in the stellar case that the simple bifurcation model may be flawed. A full resolution of the conflict between the CO fundamental line cores and other chromospheric diagnostics might require complex models with full treatment of the CO chemical equilibrium as suggested by Uitenbroek (2000b) for the solar case. Third, our observations show that the brightness temperature of α Boo does not change greatly between 1.4 mm and 2.8 mm. This might be evidence that the chromospheric temperature structure is comparatively flat between the corresponding depths of formation.

Our second objective was to use millimeter data to furnish an independent test of the 1–200 μm stellar calibration as represented by the assumption of purely photospheric radiation in these cool, normal giants. We conclude that α Tau is well-modeled purely by a photosphere to about 150–170 μm, and very likely through the longest filter relevant to ISOPHOT (C200). α Boo is well-modeled by a one-component atmosphere as far as at least 125 μm but submillimeter measurements are essential to establish its behavior beyond this wavelength and below 1.4 mm.

Our third objective was the desire to tie together flux calibrations in the infrared and millimeter. Note that this link is highly desirable now that one can observe many objects from the optical/near-infrared, through the thermal and far-infrared, and sub-mm regions, into the mm-cm. To constrain physical processes and to model such broadband sources adequately, one must assure that there are no inherent discontinuities in the underlying calibration. When stellar mm-fluxes vindicate model calculations, this establishes a link between calibration in the two spectral regimes that can eventually be pursued from space, airborne, and ground-based instruments in the sub-mm range. We note that α Tau is observed to be only 1.17σ off (fainter than) the models at 1.4 mm. Therefore, it could be compatible with a radiative equilibrium model and, thereby, fulfil a vital role as a near-infrared to 1 mm calibrator. However, we urgently require higher S/N measurements of this star at 1.4 mm, and a range of submm measurements to track possible deviations from any radiative equilibrium model.

It is clear that more submillimeter and millimeter observations are needed first to better map the transition from photosphere to chromosphere in individual stars and second to see how that differs from star to star. The first goal requires better wavelength coverage in the sub-mm to mm range to pin down the transition wavelength in individual objects. Submillimeter measurements are certainly feasible on α Tau and α Boo, and on most of the bright K-/M-giant calibrators offered by Cohen et al. (1996b), and would serve a dual purpose in helping to define the wavelength domain over which such stars could be used as calibrators for future far-infrared (e.g. SIRTF/MIPS) and sub-mm missions and instruments (e.g. Herschel/SPIRE). SCUBA would be an ideal instrument to accomplish these measurements which, for an entire set of infrared-bright K-/M-giant calibrators, would necessitate only a handful of hours.

The second goal requires a larger sample of these cool giants. We have already initiated a program of 3 mm BIMA observations of β Peg, β And, α Cet, α Hya, and γ Dra. Cohen et al. (1996b) published absolute 1.2–35 μm spectra of these; we extended all of them as far as 300 μm in January 1996, and provided these spectra to ISOPHOT. Most were measured absolutely by MSX (Cohen et al. 2001) and thereby validated in the 4–21 μm region. We plan to continue this 3-mm program and hopefully to extend it to 1-mm measurements of the same stars. However, the full scope of our study of cool giants also requires measurements of coronal and non-coronal objects, a path followed by Drake & Linsky (1986).

Finally, time variations are important. Robinson et al. (1998) found large variations (by a factor of ~2) in the near-UV continuum flux of α Tau between observations separated by years. Interestingly, this is another wavelength region which samples the same stellar layers as the mm-fluxes. We are considering whether (sub)millimeter time sampling of any of these cool giants might also be of value. Note that our BIMA measurements of α Tau span a period of just over 3 yr, during which time we have seen no statistically significant variation in 3-mm flux density above the 1σ level. However, it is perhaps curious that this star has never formally been as bright at 3 mm as during our first epoch of data (late

1997: 17 mJy) while all subsequent measurements have yielded essentially identical values (~12-13 mJy). A similar situation might obtain for α Boo which was at its formal faintest 3-mm flux level in late 1997 and has been brighter since then (again only at the 1σ level).

We wish to thank Bertrand Plez for computing an α Tau model for our particular set of input parameters and Ruth Peterson for the extended version of the Peterson et al. (1993) α Boo model. Their help is greatly appreciated. It is a pleasure to thank Bernhard Schulz, Ullie Klaas, and Phil Richards of the ISOPHOT team for sending us the complete mission archive of PHOT calibrations that compare measured source brightness with predicted and data on their validation of OLP10 as it relates to α Boo's spectrum. MC acknowledges support for this work through subcontract UF99025 between the University of Florida and UC Berkeley, supporting the calibration of ISOPHOT. DFC gratefully acknowledges access to the resources of the NASA Advanced Supercomputing (NAS) Division, NASA/Ames Research Center, Moffett Field, CA, as well as the support of the NAS Division Chief William J. Feiereisen and NAS Branch Chiefs Dochan Kwak and William W. Thigpen. SGI/Cray C90 supercomputer cycles for this research were provided through the Consolidated Supercomputing Management Office (CoSMO) at NASA/Ames. This material is based upon work by DFC and DG supported by the National Aeronautics and Space Administration under NRA-99-01-ADP-073 issued through the Astrophysics Data Program. We acknowledge support for BIMA through NSF grant AST 9981308.

REFERENCES

Altenhoff, W. J., Huchtmeier, W. K., Schmidt, J., Schraml, J. B., & Stumpff, P. 1986, A&A, 164, 227

Altenhoff, W. J., Thum, C., & Wendker, H. J. 1994, A&A, 281, 161

Ayres, T.R., Brown, A., Harper, G.M., Bennett, P.D., Linsky, J.L., Carpenter, K.G., & Robinson, R.D. 1997, ApJ, 491, 876

Ayres, T.R. & Linsky, J.L. 1975, ApJ, 200, 660

Ayres, T.R. & Rabin, D. 1996, ApJ, 460, 1042

Ayres, T.R., Testerman, L. & Brault, J.W. 1986, ApJ, 304, 542

Avrett, E. H., Hoeflich, P., Uitenbroek, H. & Ulmschneider, P. 1996, in "Cool Stars, Stellar Systems, and the Sun: Ninth Cambridge Workshop", Astronomical Society of the Pacific Conference Series, vol. 109, Eds, R . Pallivicini and A. K. Dupree, p.105. (San Francisco: Astronomical Society of the Pacific)

Blackwell, D.E., Lynas-Gray, A.E., & Petford, A.D. 1991, A&A, 245, 567

van der Bliek, N.S., Gustafsson, B. & Eriksson, K. 1996, å, 309, 849

Clegg, P. E. et al. 1996, A&A, 315, L38

Carbon, D.F., Cohen, M., Morris, P., Hayward, T., & Goorvitch, D. 2002, AJ, in preparation.

Carbon, D.F., Langer, G.E., Butler, D., Kraft, R.P., Trefzger, Ch.F., Suntzeff, N.B., Kemper, E., & Romanishin, W. 1982, ApJS, 49, 207

Carpenter, K.G., Brown, A., & Stencel, R.E. 1985, ApJ, 289, 676

Cohen, M. 1998, AJ, 115, 2092

Cohen, M. & Davies, J. K. 1995, MNRAS, 276, 715

Cohen, M., Hammersley, P.L., & Egan, M.P. 2000, AJ, 120, 3362

Cohen, M., Walker, R.G., Barlow, M.J., & Deacon, J.R., 1992a, AJ, 104, 1650

Cohen, M., Walker, R.G., Carter, B., Hammersley, P., Kidger, M., & Noguchi, K., 1999, AJ, 117, 1864

Cohen, M., Walker, R.G., Jayaraman, S., Barker, E., & Price, S.D. 2001, AJ, 121, 1180

Cohen, M., Walker, R. G., & Witteborn, F. C. 1992b, AJ, 104, 2030

Cohen, M., Witteborn, Bregman, J. D., Wooden, D.H., Salama, A., and Metcalfe, L. 1996, AJ, 112, 241

Cohen, M., Witteborn, F. C., Carbon, D. F., Augason, G. C., Wooden, D.H., Bregman, J. D., & Goorvitch, D. 1992c, AJ, 104, 2045

Cohen, M., Witteborn, F. C., Carbon, D. F., Davies, J. K., Bregman, J. D., & Wooden, D. H. 1996b, AJ, 112, 2274

Cohen, M., Witteborn, F.C., Walker, R.G., Bregman, J.D., & Wooden, D.H. 1995, AJ, 110, 275

Drake, S. A. & Linsky, J. L. 1986, AJ, 91, 602

Dreher, J.W. & Welch, W.J. 1983, AJ, 88, 1014

Egan, M.P. et al. 1999, "The Midcourse Space Experiment Point Source Catalog Version 1.2 Explanatory Guide", Air Force Research Laboratory Technical Report, AFRL-VS-TR 1999-1522

Engelke, C. W. 1992, AJ, 104, 1248

Griffin, M. & Orton, G. 1993, Icarus, 105,537

ESA 1997, The Hipparcos and Tycho Catalogues, ESA SP-1200, or http://astro.estec.esa.nl/Hipparcos/catalog.html

Gry, C. et al 2000, in "The ISO Handbook, V.4: LWS - The Long-Wavelength Spectrometer", available at http://www.iso.vilspa.esa.es/manuals/HANDBOOK/IV/lws_hb/

Hammersley, P.L. et al. 1998, A&AS, 128, 207

Harris, M.J. & Lambert, D.L. 1984, ApJ, 285, 674

Heasley, J.N., Ridgway, S.T., Carbon, D.F., Milkey, R.W. & Hall, D.N.B. 1978, ApJ, 219, 970

Kalkofen, W. 2001, ApJ, 557, 376

Kelch, W.L., Linsky, J.L., Basri, G.S., Chiu, H.-Y., Chang, S.-H., Maran, S.P., & Furenlid, I. 1978, ApJ, 220, 962

Kessler, M.F. et al. 1996, A&A, 315, L27

Lemke, D. et al. 1996, A&A, 315, L64

Lim, T., Swinyard, B.M., Liu, X.-W., Burgdorf, M., Gry, C., Pezzuto, S., & Tommasi, E. 1997, "First ISO Workshop on Analytical Spectroscopy", eds. A.M. Heras, K. Leech, N.R. Trams & M. Perry, ESA SP-419, pg. 281

Linsky, J.L., & Haisch, B.M. 1979, ApJ, 229, L27

McMurry, A.D. 1999, MNRAS, 302,37

McMurry, A.D. & Jordan, C. 2000, MNRAS, 313, 423

Mill, J. et al. 1994, AIAA, 31, 900

Mitchell, K. J. et al. 1996, in "Unveiling the Cosmic Background", ed. E. Dwek (AIP, CP 348), p.301

Muller, T.G. & Lagerros, J.S.V. 1998, A&A, 338, 340

Murakami, H. et al. 1996, PAS Japan, 48, L41

O'Brien, G. & Lambert, D.L. 1979, ApJ, 229, L33

O'Brien, G. & Lambert, D.L. 1986, ApJS, 62, 899

Orton, G., Burgdorf, M., Davis, G., Sidher, S., Griffin, M., Swinyard, B., & Feuchtgruber, H. 2000, AAS, DPS meeting #32, #11.06

Peterson, R.C. 1995, private communication

Peterson, R.C., Dalle Ore, C.M.& Kurucz, R.L. 1993, ApJ, 404, 333.

Plez, B. 1999, private communication.

Plez, B., Brett, J.M. & Nordlund, A. 1992, A&A, 256, 551.

Quirrenbach, A., Mozurkewich, D., Buscher, D.F., Hummel, C.A., & Armstrong, J.T. 1996, A&A, 312, 160

Reid, M.J. & Menten, K.M. 1997, ApJ, 476, 327

Richards, P. 2001, in "The Calibration Legacy of the ISO Mission", ed. L. Metcalfe (ESA SP-481), in press

Ridgway, S.T., Jacoby, G.H., Joyce, R.R., Siegel, M.J., & Wells, D.C. 1982, AJ, 87, 1044

Robinson, R.D., Carpenter, K.G., & Brown, A. 1998, ApJ, 503, 396

Schaeidt, S. et al. 1996, A&A, 315, L55

Schulz, B. 2001, in "The Calibration Legacy of the ISO Mission", ed. L. Metcalfe (ESA SP-481), in press

Schulz, B. et al. 2001, submitted to A&A

Sidher, S.D., Swinyard, B M., Griffin, M.J., Orton, G.S., Burgdorf, M., & Lim, T.L. 2001, "The calibration legacy of the ISO Mission", eds. L. Metcalfe and M.F.K. Kessler, ESA SP-481 (in press)

Smith, V.V. & Lambert, D.L. 1985, ApJ, 294, 326

Smith, V.V. & Lambert, D.L. 1990, ApJS, 72, 387

Swinyard, B. et al. 1996, A&A, 315, L43

Tsuji, T. 2000, ApJ, 540, 99

Uitenbroek, H. 2000, ApJ, 531, 571

Uitenbroek, H. 2000, ApJ, 536, 481

Vernazza, J. E., Avrett, E. H., & Loeser, R. 1973, ApJ, 184, 605

Vernazza, J. E., Avrett, E. H., & Loeser, R. 1976, ApJS, 30, 1

Welch, W. J., & Gibson, J. 2001, in preparation

Wendker, H. 1995, Vizier Catalog II/199A

Wiedemann, G., Ayres, T. Y., Jennings, D. E., & Saar, S. H. 1994, ApJ, 423, 806

Wright, E. L. 1976, ApJ, 210, 250

Wrixon, G. T., Welch, W. J., & Thornton, D. T. 1971, ApJ, 169, 171

This manuscript was prepared with the AAS LaTeX macros v5.0.

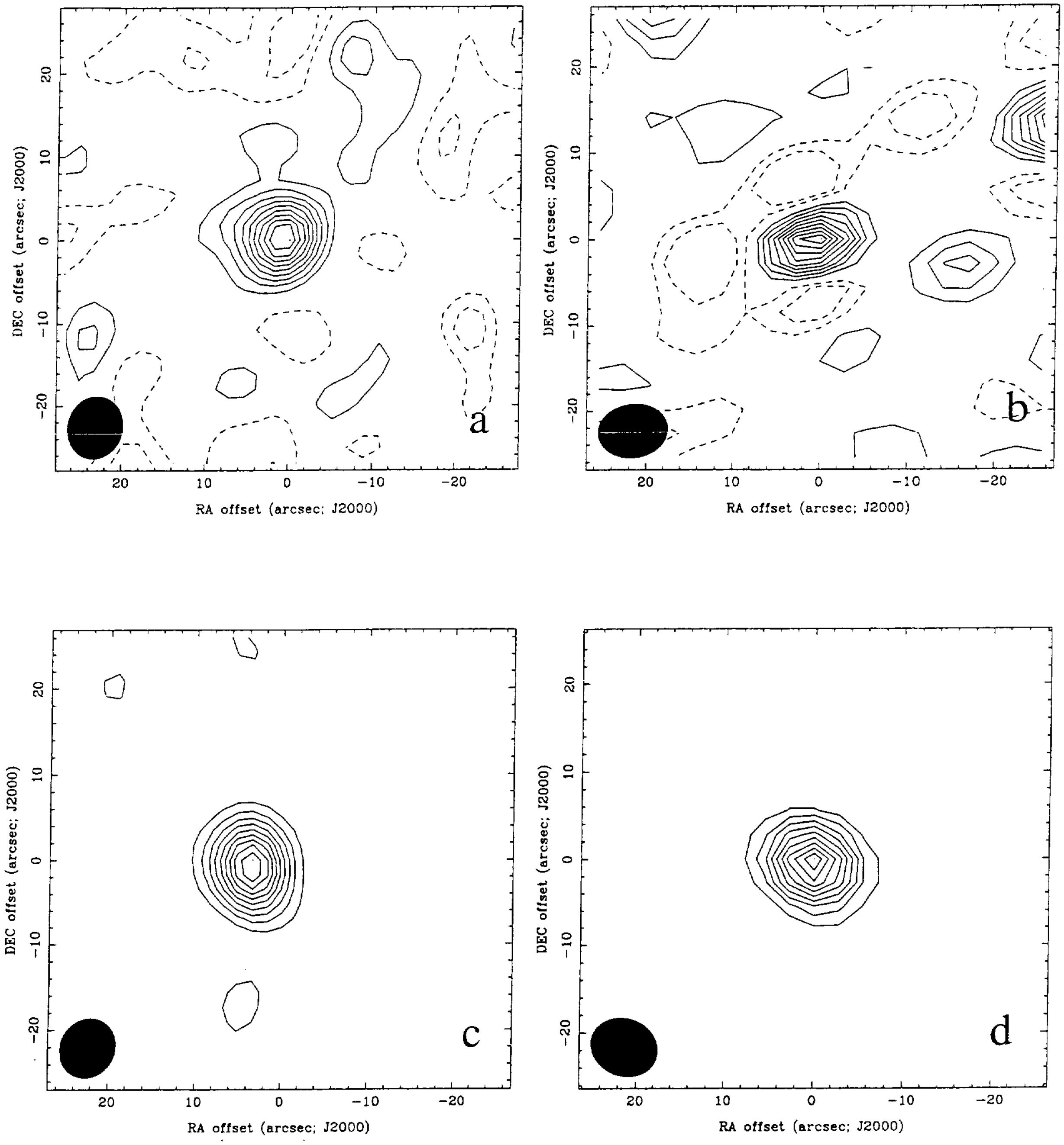

Fig. 1.— Images of both stars at 3 mm and 1 mm constructed from the combination of all available data. In each plot, contours are given at -20, -10, 10, 20, 30, 40, 50, 60, 70, 80, 90, 100% of the peak flux density. a) α Tau at 3 mm with a 13.97 mJy peak. b) α Tau at 1 mm with a 25.78 mJy peak. c) α Boo at 3 mm with 20.09 mJy peak. The offset of the peak from the stellar position after allowance for proper motion is caused by the process of self-calibration. d) α Boo at 1 mm with a 83.5 mJy peak.

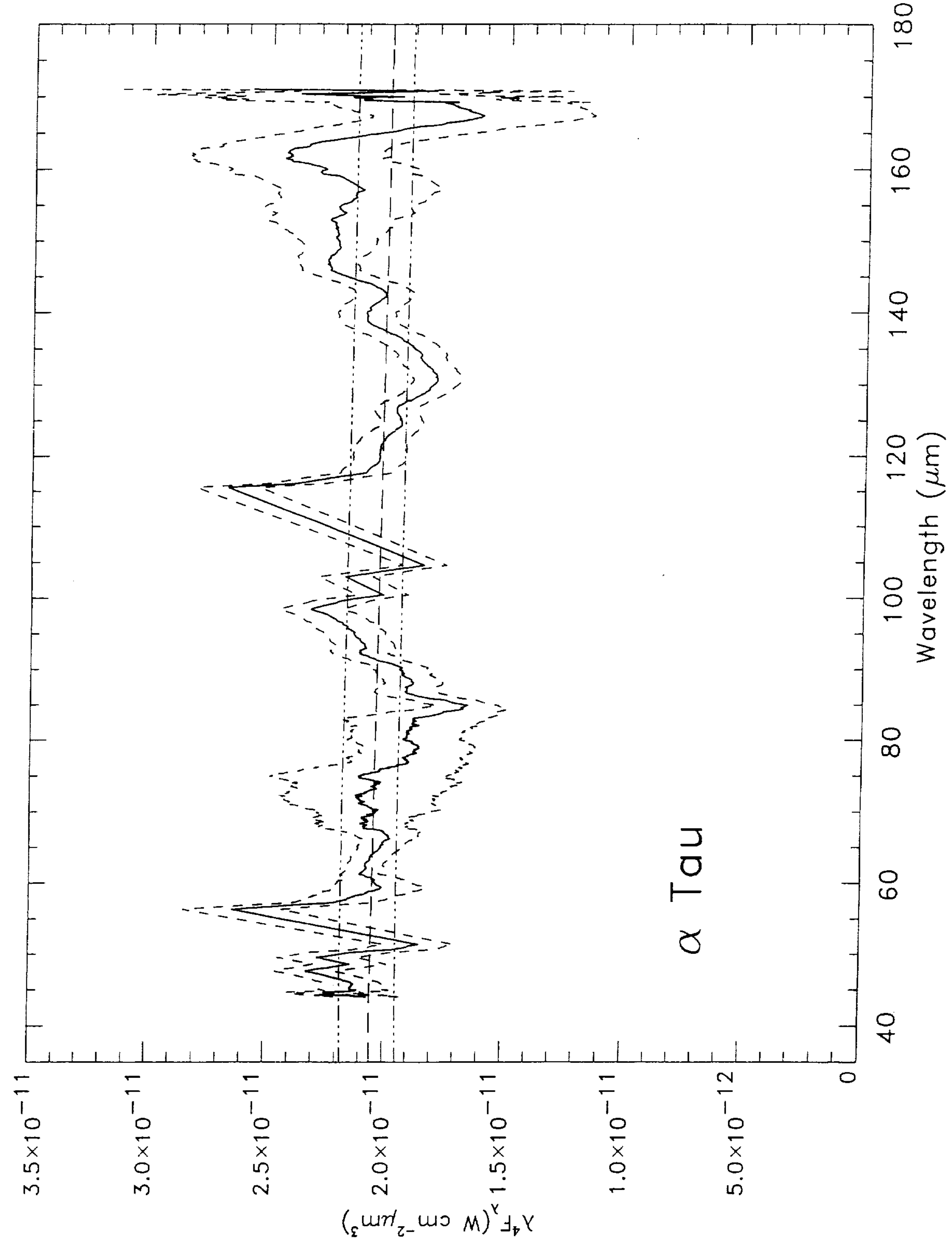

Fig. 2.— LWS spectrum of α Tau showing the mean observed spectrum (solid line) after boxcar smoothing, and the mean$\pm3\sigma$ bounds (short-dashed lines), compared with the Plez model continuum spectrum (long-dashed lines), and with the mean$\pm1\sigma$ bounds on the old SED provided to ISOPHOT in 1996 (dash-triple-dotted lines).

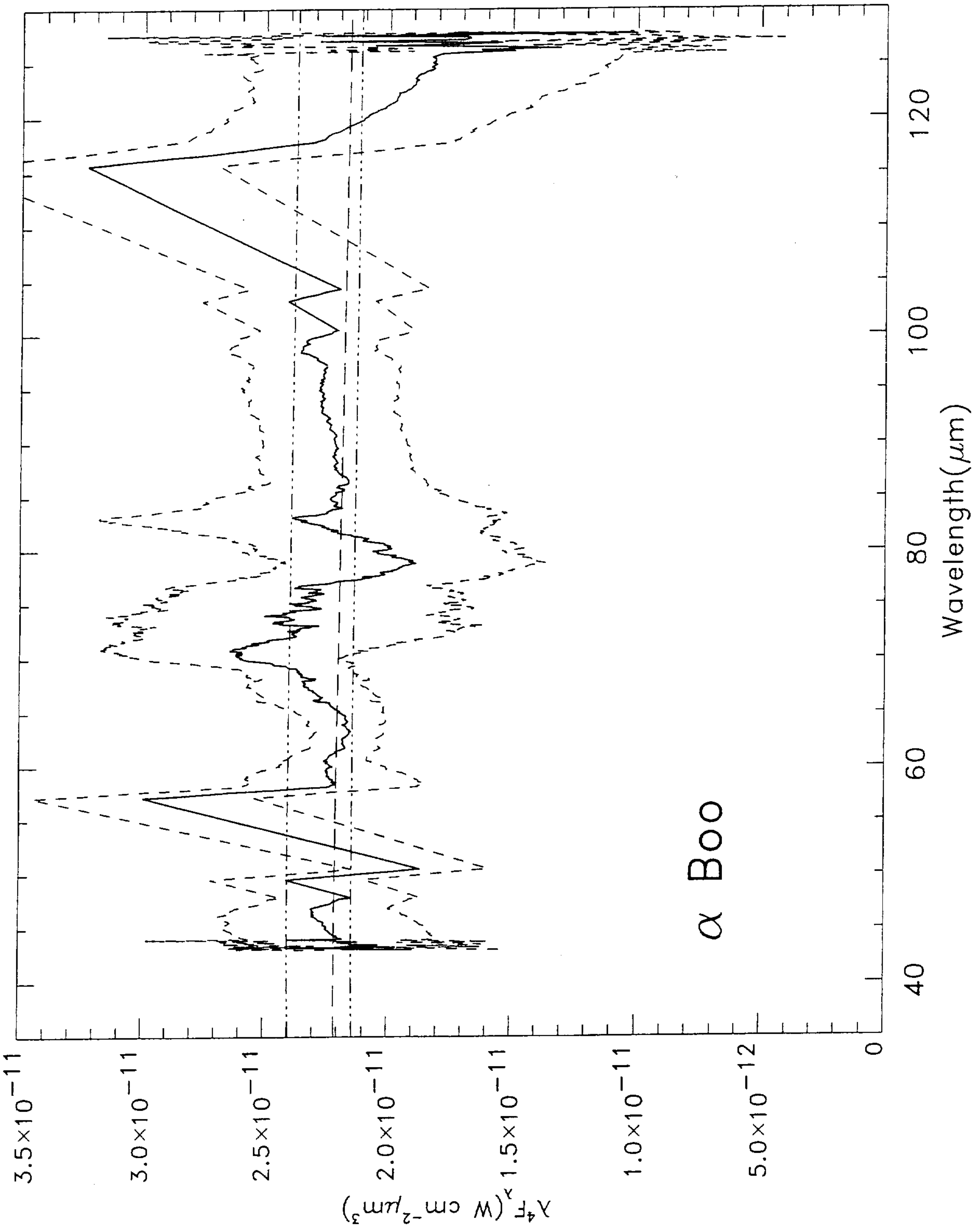

Fig. 3.— LWS spectrum of α Boo showing the mean observed spectrum (solid line) after boxcar smoothing, and the mean$\pm2\sigma$ bounds (short-dashed lines), compared with the PDK model continuum spectrum (long-dashed lines), and with the mean$\pm1\sigma$ bounds on the old SED provided to ISOPHOT in 1996 (dash-triple-dotted lines).

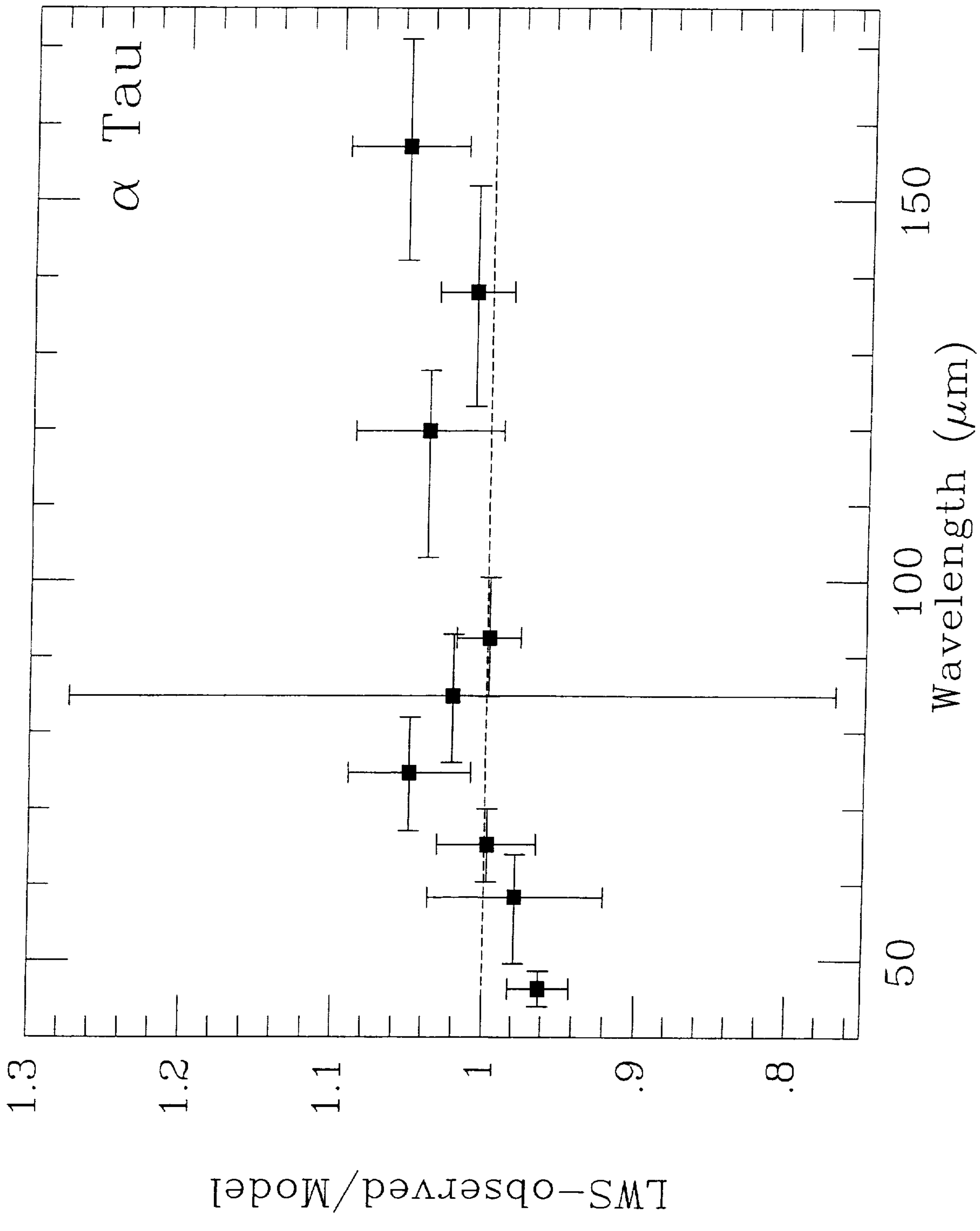

Fig. 4.— Ratio of LWS observed flux densities for each independent detector to those predicted by the Plez model for α Tau. Each detector result is shown as a cross, where horizontal bars represent the actual wavelength extent of the useful data, and vertical bars show the 1σ errors on the plotted weighted-mean points.

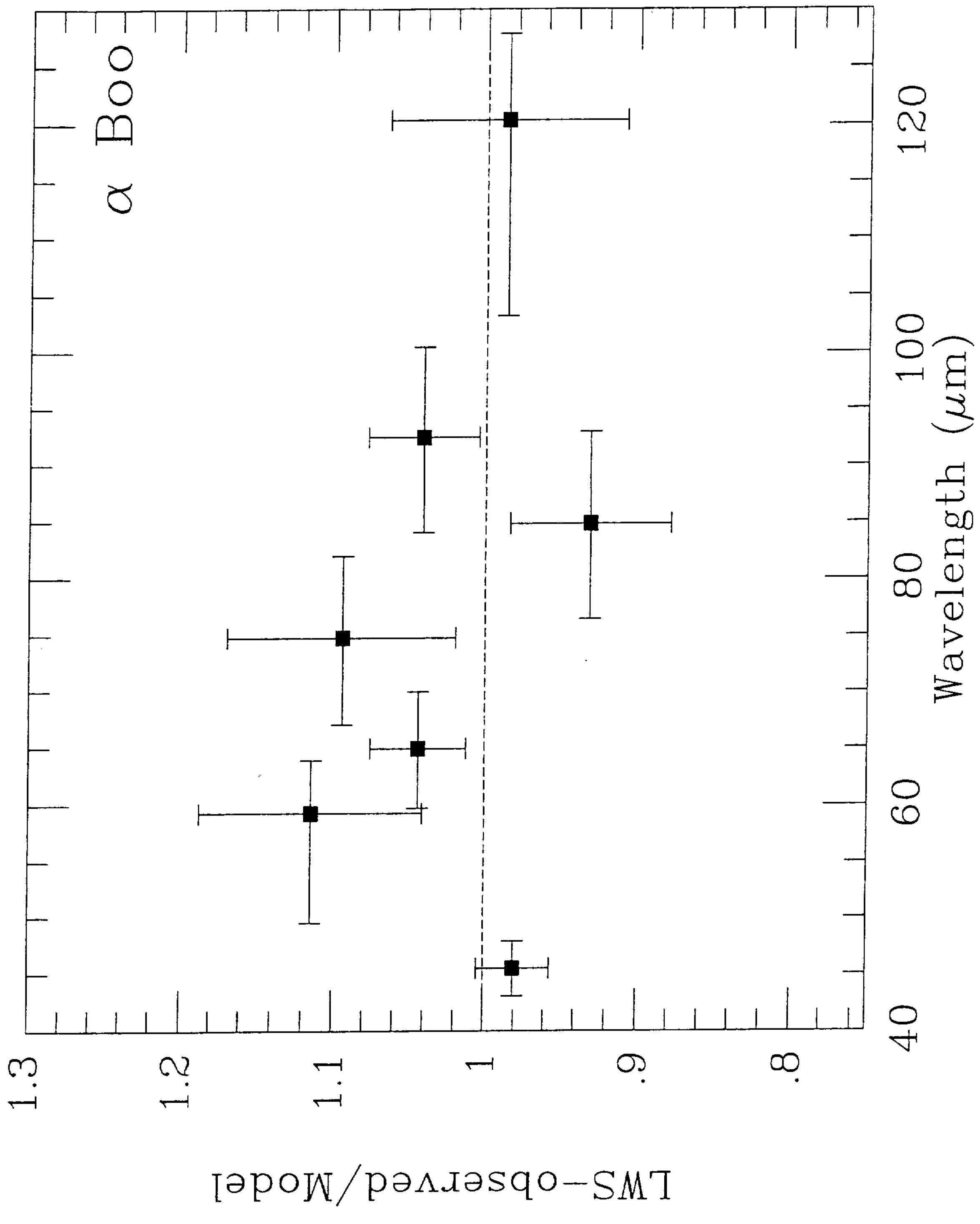

Fig. 5.— Ratio of LWS observed flux densities for each independent detector to those predicted by the PDK model for α Boo. Details as for Figure 4.

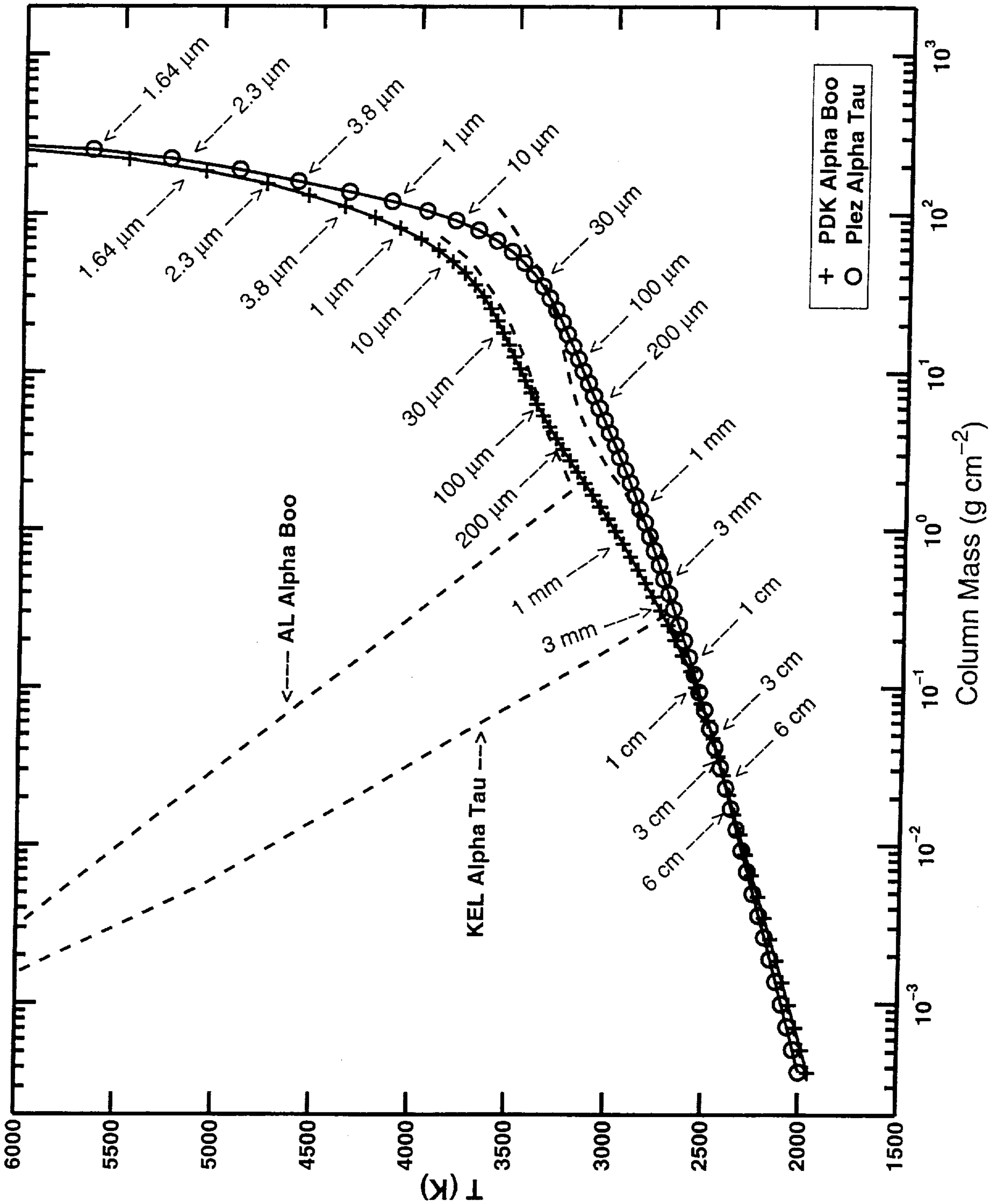

Fig. 6.— The adopted model atmosphere temperature structures for α Boo and α Tau. Arrows mark the depths at which optical depth unity is reached in the continuum at the indicated wavelengths. The upper set of arrows refers to the PDK model; the lower set, to the Plez model. For comparison, the AL and KEL chromosphere models are shown as dashed lines.

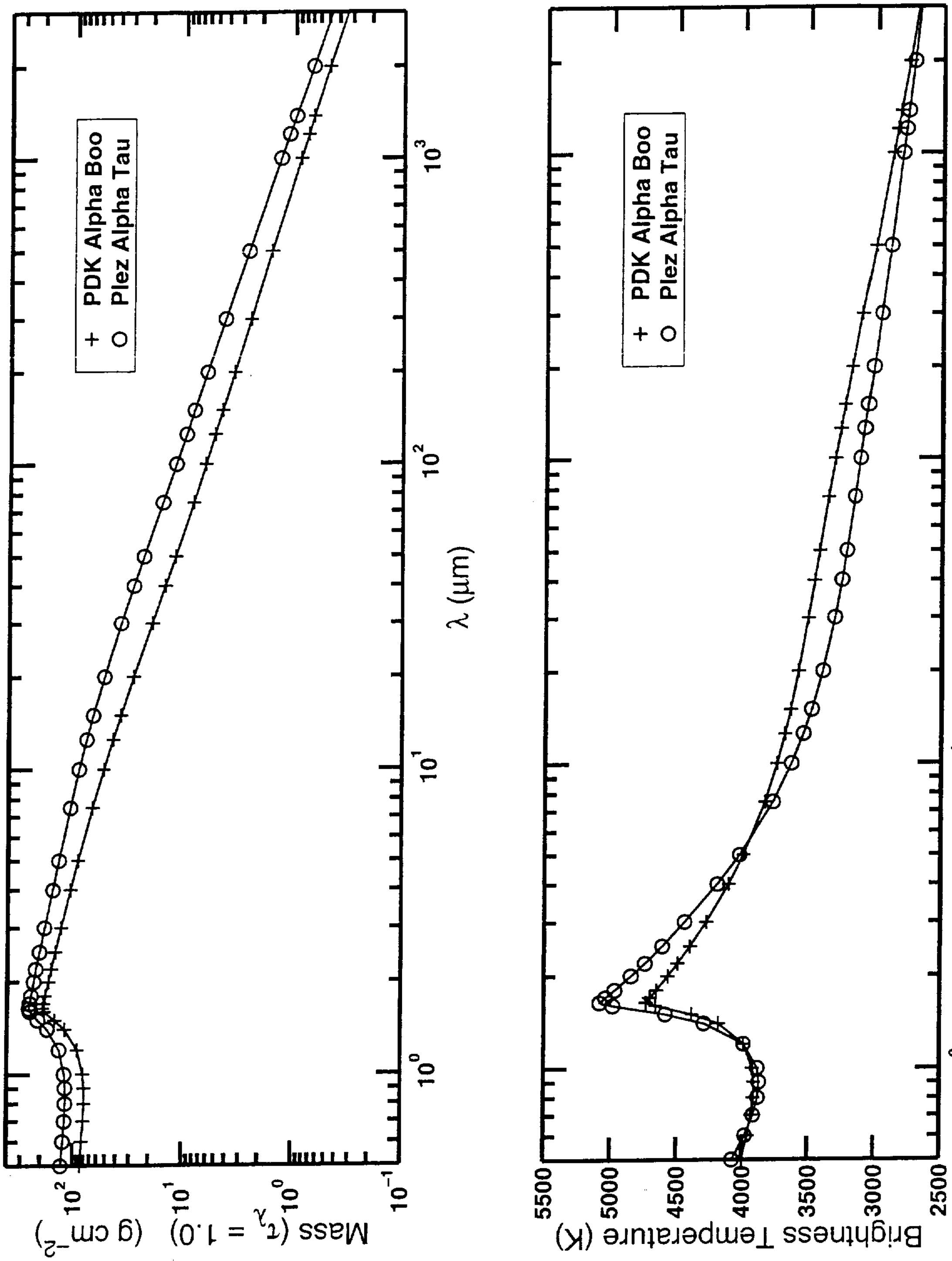

Fig. 7.— Upper panel: The column masses at which continuum optical depth unity is reached in the PDK α Boo and Plez α Tau radiative equilibrium models. Lower panel: The brightness temperatures predicted by the PDK α Boo and Plez α Tau radiative equilibrium models.

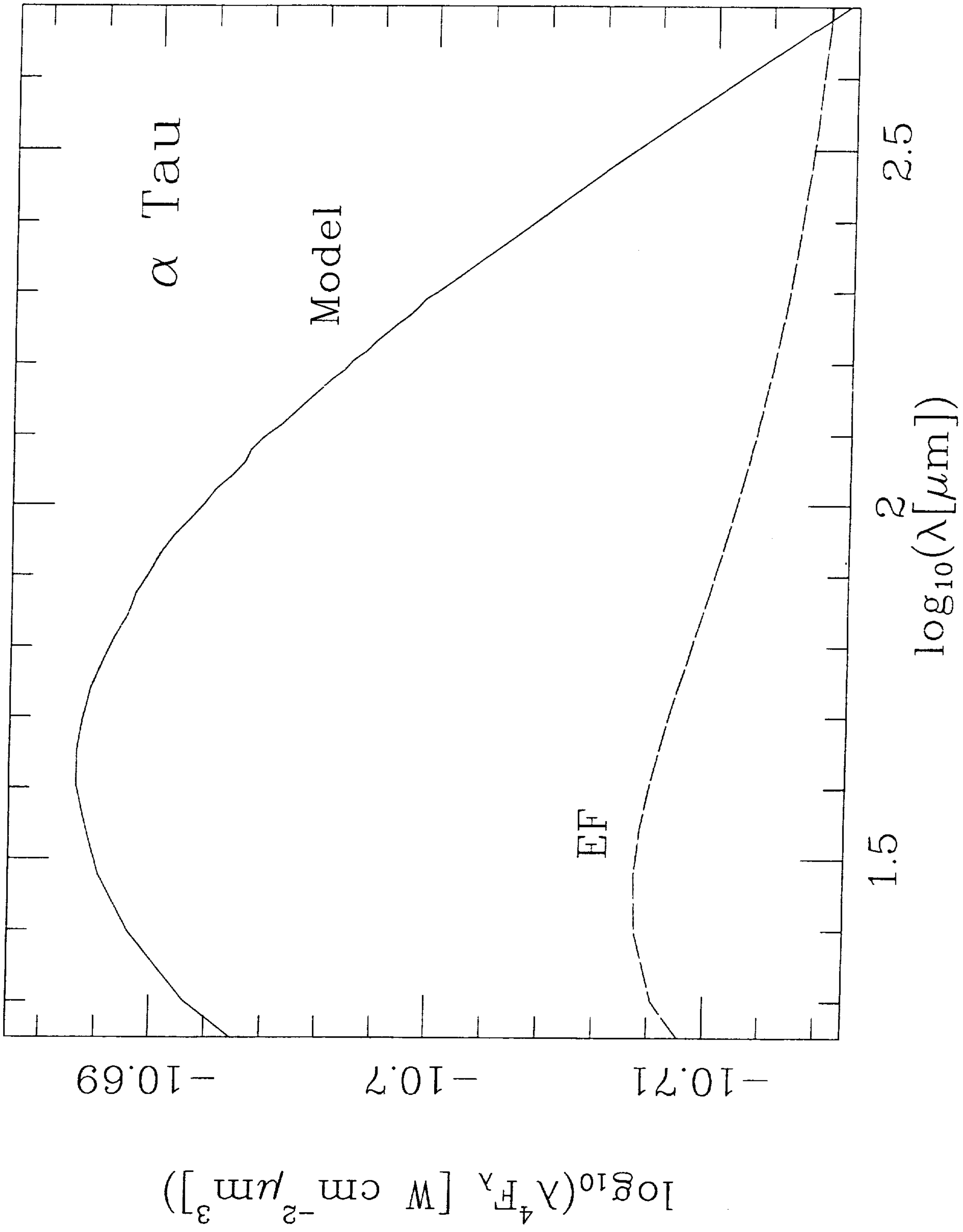

Fig. 8.— Our calculated Plez α Tau continuum spectrum compared with the function representing the Engelke continuum approximation ("EF") for this star.

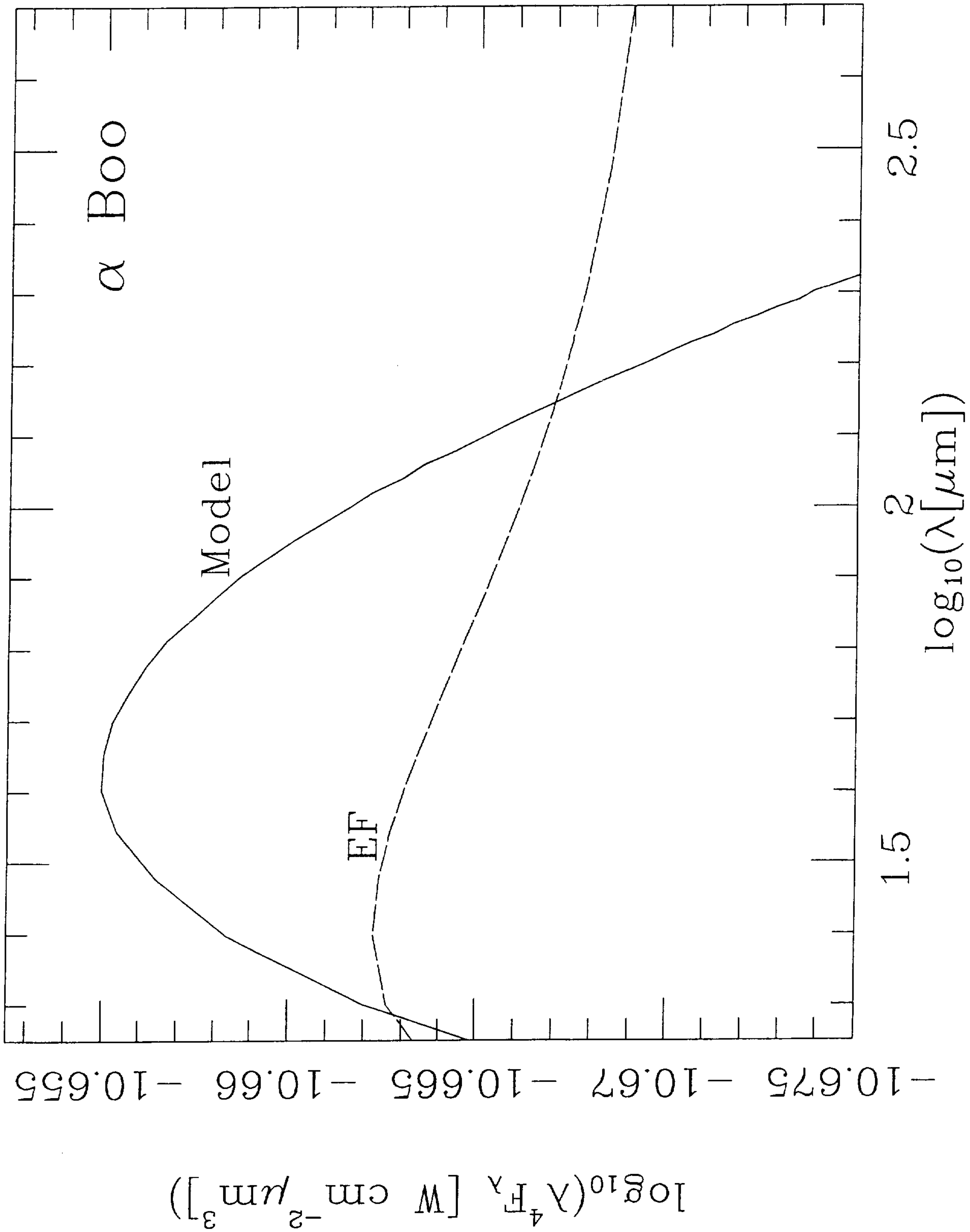

Fig. 9.— Our calculated PDK α Boo continuum spectrum compared with the Engelke continuum approximation ("EF") for this star.

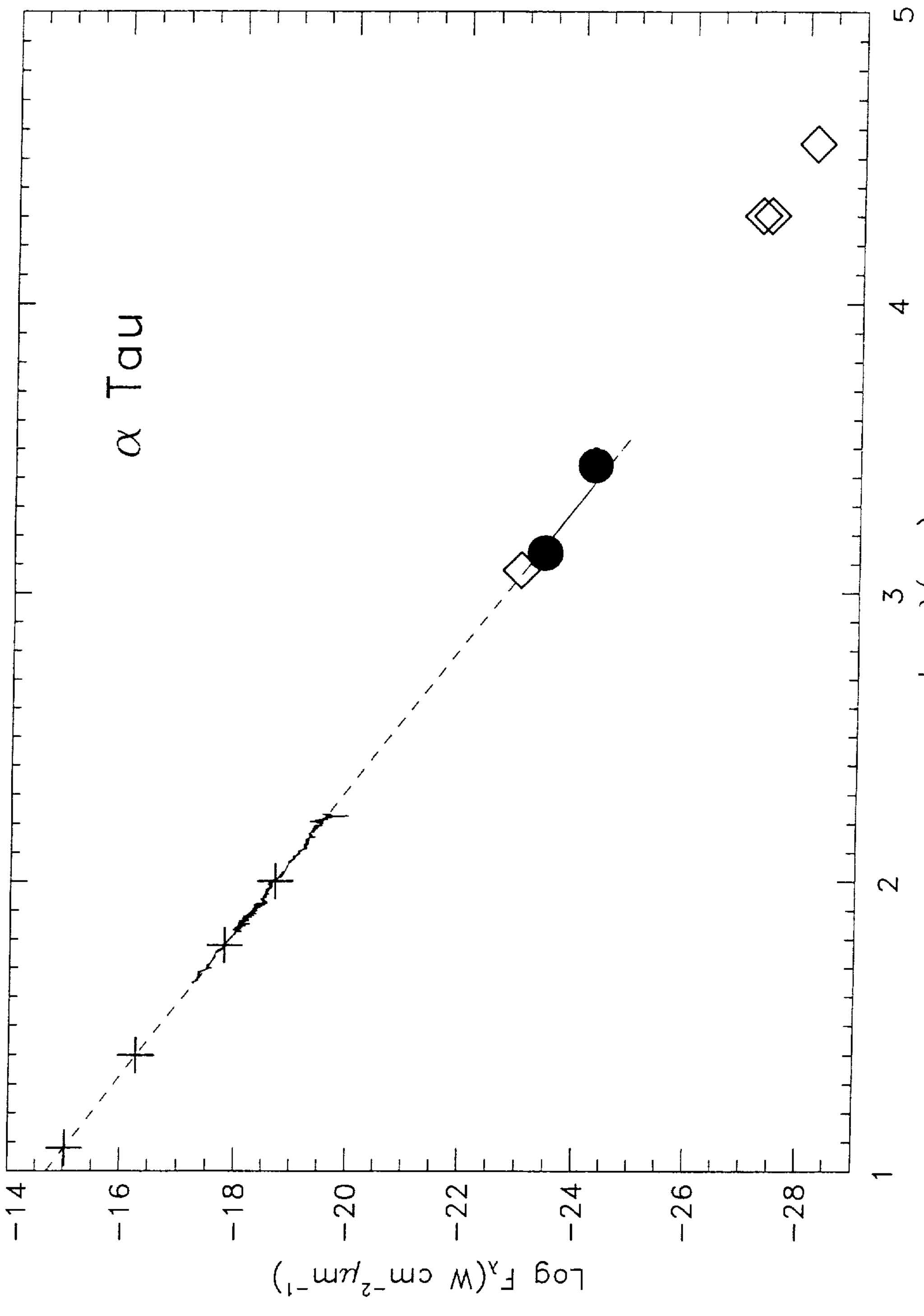

Fig. 10.— Far-infrared to cm spectrum of α Tau. Color-corrected IRAS points (crosses) are plotted together with our mm observations (filled circles), the LWS spectrum (solid), and our computed continuum spectrum (dashed line). Also shown are mm and cm data from the literature (open diamonds).

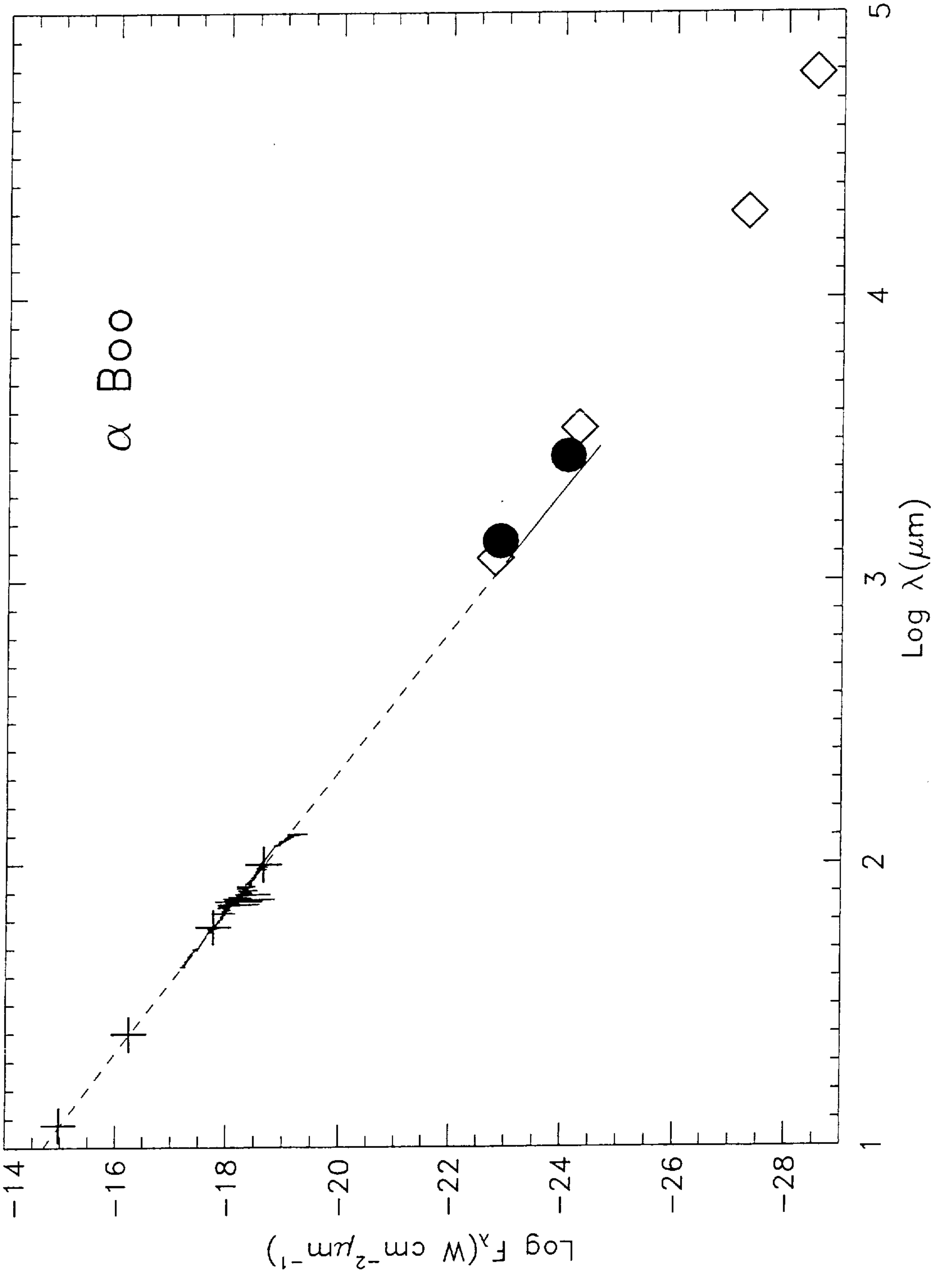

Fig. 11.— Far-infrared to mm spectrum of α Boo as for Figure 10.

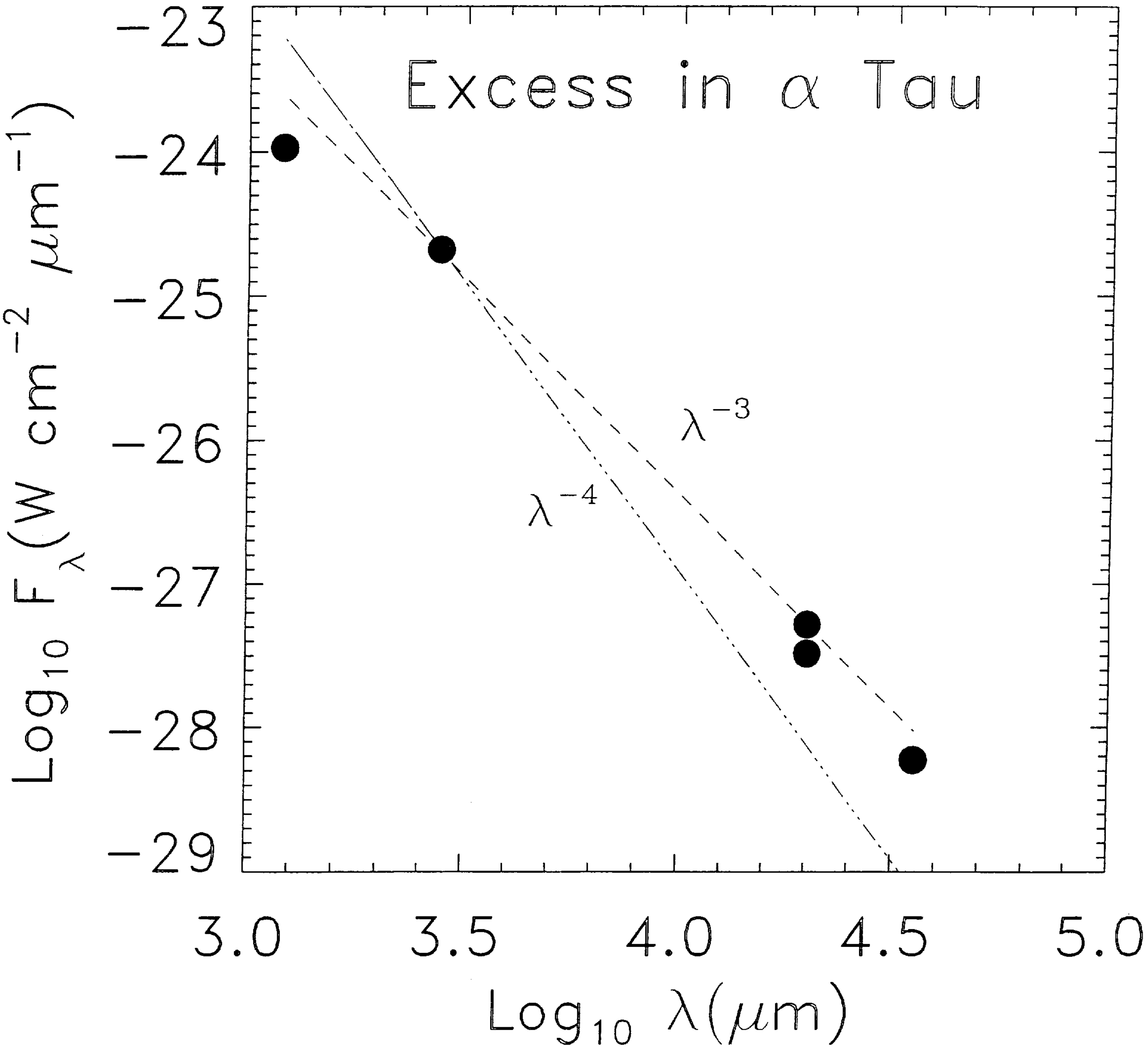

Fig. 12.— Millimeter to centimeter spectrum of the excess emission in α Tau above the Plez radiative equilibrium model, compared with λ^{-3} and λ^{-4} slopes normalized at 2.8 mm.

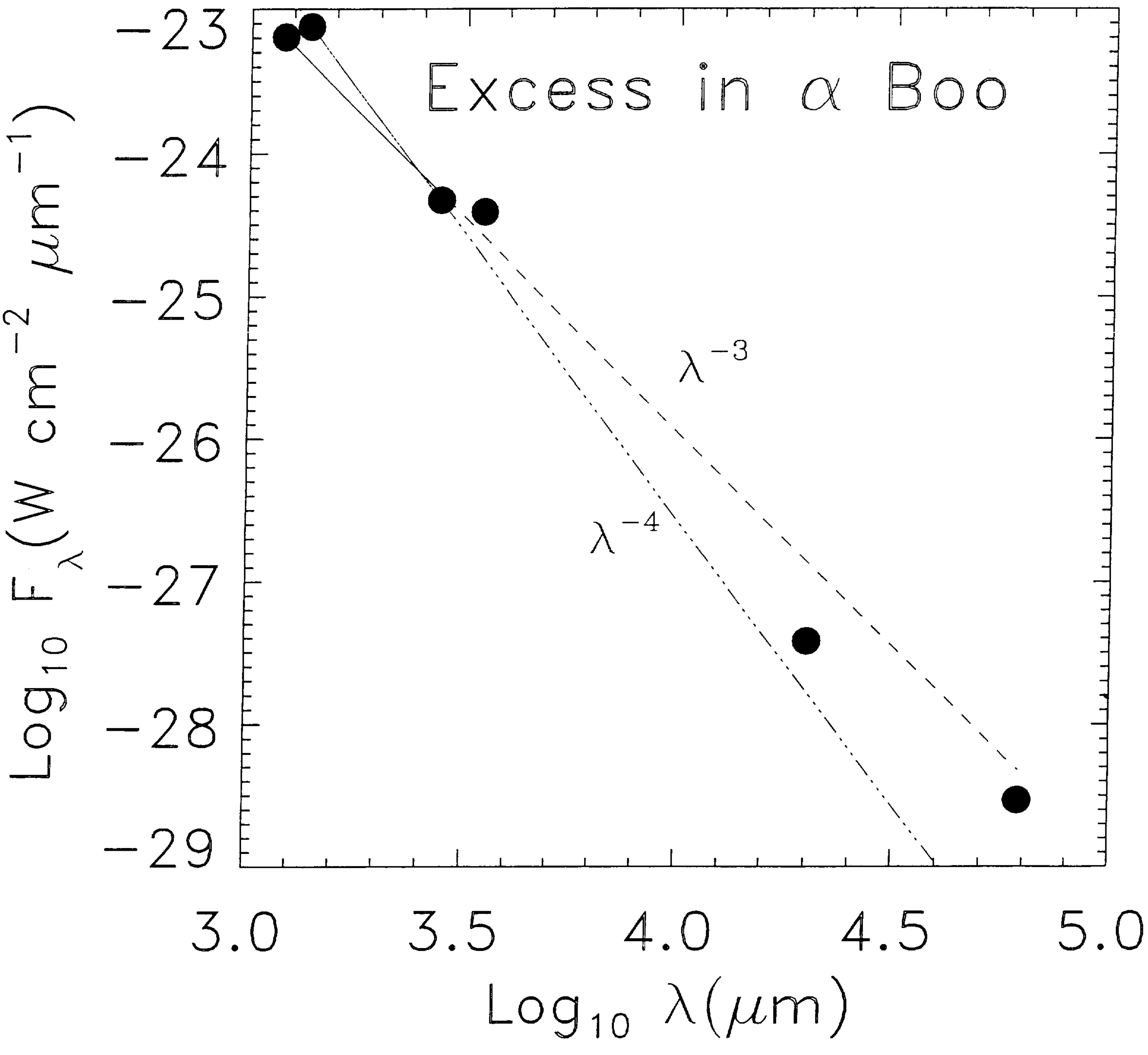

Fig. 13.— Millimeter to centimeter spectrum of the excess emission in α Boo above the PDK radiative equilibrium model, compared with λ^{-3} and λ^{-4} slopes normalized at 2.8 mm.

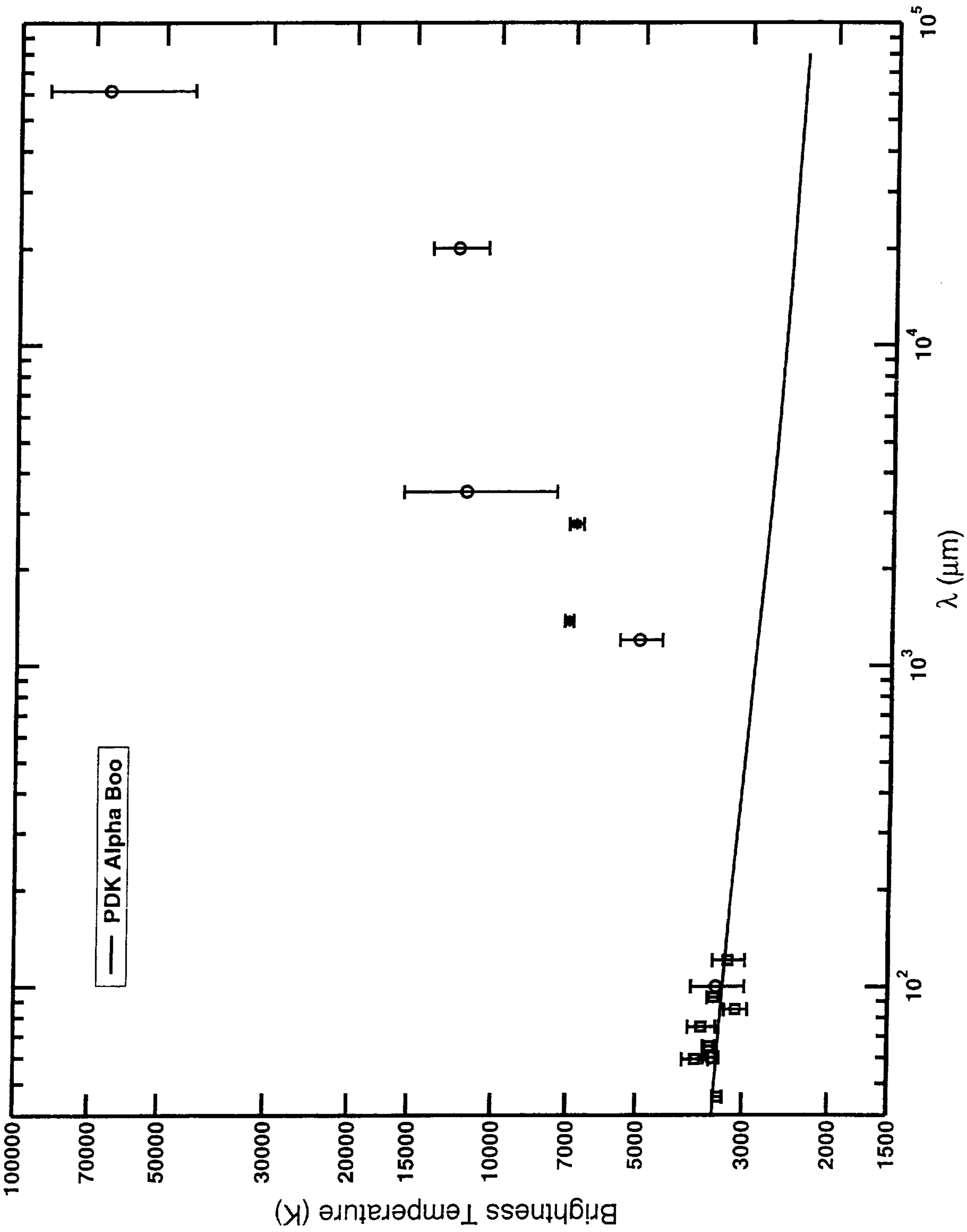

Fig. 14.— Brightness temperatures corresponding to the observed fluxes for α Boo which have been discussed in this paper. LWS observations are represented by open squares, our mm measurements by asterisks, all other observations by open circles. Error bars represent 1σ deviations in the fluxes only. Brightness temperatures predicted by the PDK model shown by a solid line.

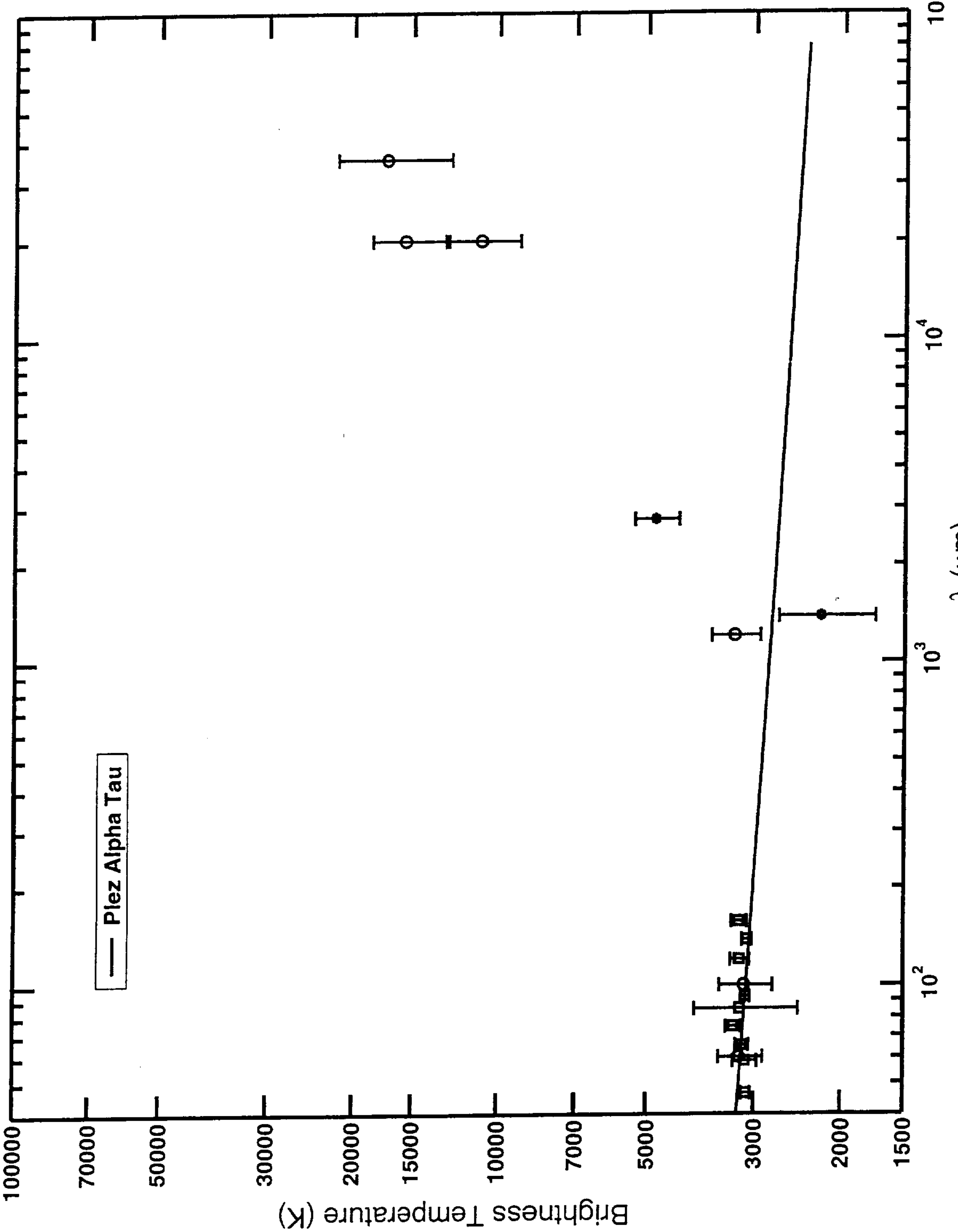

Fig. 15.— Brightness temperatures corresponding to the observed fluxes for α Tau which have been discussed in this paper. LWS observations are represented by open squares, our mm measurements by asterisks, all other observations by open circles. Error bars represent 1σ deviations in the fluxes only; errors for 2-cm and 3.6-cm points are our own estimates (see text). Brightness temperatures predicted by the Plez model shown by a solid line

TABLE 1. Journal of observations

Star	Date	Array	Frequency GHz	Time on star	Phase Ref.	Secondary Flux Ref.	Primary Flux Ref.	Traceable to Primary	Peak F_ν mJy
α Tau	14Nov97	C	106.6845	4.32 hr	0449+113	3C111	Mars,	⋯	17.14±2.19
⋯	⋯	⋯	⋯	⋯	⋯	⋯	Uranus, Neptune	⋯	⋯
α Boo	15Nov97	C	106.6845	4.22 hr	1415+133	3C111	Mars,	⋯	20.27±2.95
⋯	⋯	⋯	⋯	⋯	1357+193	⋯	Uranus, Neptune	⋯	⋯
α Boo	15Nov97	C	110.1282	4.22hr	1415+133	3C111	Mars,	⋯	18.47±2.73
⋯	⋯	⋯	⋯	⋯	1357+193	⋯	Uranus, Neptune	⋯	⋯
α Boo	15Nov97	C	Both	⋯	⋯	⋯	⋯	⋯	19.73±2.16
α Tau	06Jun98	C	106.6845	2.99hr	0449+113	3C111	Mars	⋯	13.10±3.40
α Boo	11Mar99	B	106.6845	⋯	1357+193	1415+133	⋯	Mars	24.57±1.20
α Boo	11Mar99	B	110.1282	4.37 hr	1357+193	1415+133	⋯	Mars	19.68±1.23
α Boo	11Mar99	B	Both	⋯	⋯	⋯	⋯	⋯	22.03±0.97
α Boo	12Mar99	B	106.6845	3.13 hr	1357+193	1415+133	MWC349, Mars	Mars	21.02±1.74
α Boo	12Mar99	B	110.1282	⋯	1357+193	1415+133	MWC349, Mars	Mars	18.90±1.20
α Boo	12Mar99	B	Both	⋯	⋯	⋯	⋯	⋯	19.92±1.02
α Tau	05Sep99	D	216.0982	1.85 hr	0530+135	0530+135	⋯	MWC349/Mars	24.23±6.87
α Tau	05Sep99	D	219.5418	⋯	0530+135	0530+135	⋯	MWC349/Mars	27.34±8.12
α Tau	05Sep99	D	Both	⋯	⋯	⋯	⋯	⋯	25.78±5.64
α Boo	01Jun00	D	216.0982	2.91 hr	3C273	3C273	MWC349	Mars	81.55±2.35
α Boo	01Jun00	D	219.5418	2.91 hr	3C273	3C273	MWC349	Mars	85.45±2.44
α Boo	01Jun00	D	Both	⋯	⋯	⋯	⋯	⋯	83.50±1.71
α Tau	09Dec00	C	106.6845	3.19 hr	3C111	3C111	W3OH, Mars,	⋯	12.55±2.16
⋯	⋯	⋯	⋯	⋯	⋯	⋯	Uranus	⋯	⋯
α Tau	09Dec00	C	110.1282	3.19 hr	3C111	3C111	W3OH, Mars,	⋯	12.77±2.95
⋯	⋯	⋯	⋯	⋯	⋯	⋯	Uranus	⋯	⋯
α Tau	09Dec00	C	Both	⋯	⋯	⋯	⋯	⋯	12.40±1.91
α Tau	All	All	108.40	⋯	⋯	⋯	⋯	⋯	13.97±1.46
α Tau	All	All	217.82	⋯	⋯	⋯	⋯	⋯	25.78±5.64
α Boo	All	All	108.40	⋯	⋯	⋯	⋯	⋯	20.09±0.69
α Boo	All	All	217.82	⋯	⋯	⋯	⋯	⋯	83.50±1.71

TABLE 2. Radiative models: fluxes and brightness temperatures

Frequency	Quantity	α Boo	α Tau
217.820 GHz (1.376 mm)	Observed Flux (mJy)	83.50±1.71	25.78±5.64
···	Predicted Flux (mJy)	33.43	32.38
···	|Predicted–Observed Flux|/σ(observed)	29.3	1.17
···	Observed Brightness Temperature (K)	7040±140	2200±480
···	Predicted Brightness Temperature (K)	2820	2760
108.406 GHz (2.765 mm)	Observed Flux (mJy)	20.09±0.69	13.97±1.46
···	Predicted Flux (mJy)	7.94	7.80
···	|Predicted–Observed flux|/σ(observed)	17.6	4.23
···	Observed Brightness Temperature (K)	6840±230	4810±500
···	Predicted Brightness Temperature (K)	2700	2690

TABLE 3. Radiative Models: atmospheric extents

Quantity	α Boo	α Tau
Adopted angular diameter (mas)	21.0±0.2	20.88±0.10
Adopted parallax (mas)	88.85±0.74	50.09±0.95
Deduced stellar radius (cm)	1.77×10^{12}	3.12×10^{12}
1.64 μm - 2.8 mm atmospheric thickness (cm)	4.38×10^{10}	4.22×10^{10}
Percentage of stellar radius	2.5%	1.4%

TABLE 4. Bifurcation model: fluxes and brightness temperatures

Star	Origin of flux	1.376 mm $S(1.376mm)$ mJy	 $T_B(1.376mm)$ K	2.765 mm $S(2.765mm)$ mJy	 $T_B(2.765mm)$ K
α Boo	observed	83.50	7040	20.09	6840
···	adopted cool (90%)	33.43	2820	7.94	2700
···	deduced hot (10%)	534	45000	129	43900
α Tau	observed	25.78	2200	13.97	4810
···	adopted cool (90%)	32.38	2760	7.80	2690
···	deduced hot (10%)	···	···	69.5	23900